



# Numerical simulation of critical heat flux in forced boiling of a flow in an inclined tube with different angles

Mohammad Reza Sheykhi<sup>1</sup> · Masoud Afrand<sup>2</sup> · Davood Toghraie<sup>1</sup> · Pouyan Talebizadehsardari<sup>3,4</sup>

Received: 6 October 2019 / Accepted: 6 December 2019 / Published online: 16 January 2020  
© Akadémiai Kiadó, Budapest, Hungary 2020

## Abstract

In this paper, the effect of changing tube slope on the critical heat flux for the evaporation of upward saturated flow of a liquid (water) in a near-vertical tube has been studied numerically. For this purpose, the effect of increasing the pipe slope and changing the wall temperature and the inlet fluid temperature on the volume fraction of vapor, heat transfer coefficient, heat flux and velocity profile is analyzed. In the most industrial units, boiling in diagonal channels is very important. Tube slope has an important effect on the flow stability. In practical applications, the existence of natural obstacles in the direction of transmission lines causes the orientation of these lines at different angles. The geometry of cases is a tube with 2.5 cm diameter and 100 cm length into which constant mass flow of fluid has been entered with rates of  $0.05 \text{ kg s}^{-1}$ . Because of having no changes in the third direction, the problem has been modeled two-dimensionally. Numerical simulation of fluid was done by using the RPI subcategory of boiling from the Eulerian model, and the comparison of numerical results with valid experimental data shows 14% of error. The temperature difference range of  $10 \text{ }^\circ\text{C}$  up to  $330 \text{ }^\circ\text{C}$  has been applied to the tube wall. The outcome of this study was the increase in vapor volume fraction and heat flux and decrease in heat transfer coefficient with increasing the temperature difference. Increasing the tube slope causes an increase in vapor volume fraction, heat flux and velocity profile and reduction in the temperature of the occurrence of critical heat flux.

**Keywords** Tube slope · Critical heat flux · Tube angle · Evaporation · Inclined tube · Boiling

## Introduction

In most industrial units, boiling in diagonal channels is very important. The tube slope has an important effect on flow stability. In practical applications, the existence of natural obstacles in the direction of the transmission lines causes the orientation of these lines at different angles [1–40]. Pezo and Stevanovic [41] predicted the critical heat flux in pool boiling with the two-fluid model. They found that the decrease in

nucleation site density leads to the reduction in critical heat flux values. Konishi and Mudawar [42] reviewed flow boiling and critical heat flux in microgravity. They found that there is a severe shortage of useful correlations, mechanistic models and computational models which compromise readiness to adopt flow boiling in future space systems. Sadaghiani and Kosar [43] investigated the effects of diameter and length on high mass flux subcooled flow boiling in horizontal microtubes. They concluded that with the increase in mass flux, an enhancement in boiling heat transfer is observed, implying convective heat transfer effects on flow boiling along with the nucleate boiling. Lee and Lee [44] investigated the critical heat flux enhancement of pool boiling with adaptive fraction control of patterned wettability. In this paper, the effects of size and concentration of hydrophobic dots were analyzed by observing the tendency of CHF, superheat and local Nusselt number. Fang et al. [45] reviewed the heat transfer and critical heat flux of nanofluid boiling. Chernyavskiy and Pavlenko [46] simulated the heat transfer and critical heat fluxes at unsteady heat generation in falling wavy liquid films. In this work, the dependency of characteristic heat flux density of boiling

✉ Pouyan Talebizadehsardari  
ptsardari@tdtu.edu.vn

<sup>1</sup> Department of Mechanical Engineering, Khomeinishahr Branch, Islamic Azad University, Khomeinishahr, Iran

<sup>2</sup> Department of Mechanical Engineering, Najafabad Branch, Islamic Azad University, Najafabad, Iran

<sup>3</sup> Department for Management of Science and Technology Development, Ton Duc Thang University, Ho Chi Minh City, Vietnam

<sup>4</sup> Faculty of Applied Sciences, Ton Duc Thang University, Ho Chi Minh City, Vietnam

suppression and total local evaporation suppression on the inlet Reynolds number was also presented. Sato and Niceno [47] simulated the boiling flow using an interface tracking method in the framework of computational fluid dynamics. The computed heat transfer coefficient agreed well with the measured value, demonstrating the capability of the described simulation method to predict boiling heat transfer for the wide range of boiling regimes. Ferrari et al. [48] analyzed slug flow boiling in square microchannels. They found that the flow configuration in the square channel undergoes a substantial transition as the capillary number is reduced. As the bubble shape becomes non-axisymmetric, the interface curvature changes sign along the sides of the cross section, and the liquid film thickness varies considerably along the perimeter of the cross section. Jian-sheng et al. [49] simulated the pool boiling with special heated surfaces. They concluded that the vessel with the modified heated surface has a better heat transfer performance compared to that of the plain heated surface. Furthermore, the modified heated surface with downward-facing hemispheres has the best heat transfer performance and the lowest critical heat flux (CHF) among the present three heated surfaces. Cheng et al. [50] simulated the single bubble growth in subcooled boiling water. Their results were compared with the existing datum of the visual experiment in the previous literature to verify the validity of the simulation.

In this investigation, the effect of changing the tube slope on critical heat flux for the evaporation of upward saturated flow of a liquid (water) in a near-vertical tube has been studied numerically. The effect of increasing the slope of the pipe and changing the wall temperature and the inlet fluid on the variables vapor volume fraction, heat transfer, coefficient heat flux and velocity profile is analyzed.

## General equations

### Volumetric fractions

The volume of phase  $q$  is defined as follows:

$$V_q = \int_V \alpha_q dV \quad (1)$$

and

$$\sum_{q=1}^n \alpha_q = 1 \quad (2)$$

The effective density of the phase  $q$  is equal to:

$$\hat{\rho}_q = \alpha_q \rho_q \quad (3)$$

where  $\rho_q$  is the physical density of the phase  $q$ .

### Continuity equation

The equation of mass conservation for the phase  $q$  is equal to:

$$\frac{\partial}{\partial t} (\alpha_q \rho_q) + \nabla \cdot (\alpha_q \rho_q \vec{v}_q) = \sum_{p=1}^n (\dot{m}_{pq} - \dot{m}_{qp}) + S_q \quad (4)$$

where  $\vec{v}_q$  is the velocity of phase  $q$ ,  $\dot{m}_{pq}$  describes the mass transfer from  $p$  to  $q$  phase and  $\dot{m}_{qp}$  describes the mass transfer from  $q$  to  $p$  phase. The source term  $S_q$  on the right side of Eq. (3) is zero, which can be defined for that value or function, if necessary.

### Energy equation

$$\begin{aligned} \frac{\partial}{\partial t} (\alpha_q \rho_q h_q) + \nabla \cdot (\alpha_q \rho_q \vec{u}_q h_q) = & -\alpha_q \frac{\partial p_q}{\partial t} + \bar{\tau}_q : \nabla \vec{u}_q - \nabla \cdot \vec{q}_q + S_q \\ & + \sum_{p=1}^n (\dot{Q}_{pq} + \dot{m}_{pq} h_{pq} - \dot{m}_{qp} h_{qp}) \end{aligned} \quad (5)$$

where  $h_q$  is the special enthalpy of phase  $q$ ,  $\vec{q}_q$  is the heat flux,  $S_q$  is the energy source,  $\dot{Q}_{pq}$  is the heat exchange intensity between  $p$  and  $q$  phases and  $h_{pq}$  is the interphase enthalpy (e.g., vapor at dripping temperature in evaporation). Heat exchange between phases should be in accordance with the local equilibrium conditions:  $\dot{Q}_{pq} = -\dot{Q}_{qp}$  and  $\dot{Q}_{qq} = 0$ .

### Heat transfer

The internal energy balance of the phase  $q$  is defined by the enthalpy of the phase as follows:

$$H_q = \int c_{p,q} dT_q \quad (6)$$

where  $c_{p,q}$  is the specific heat of phase  $q$ .

### Heat exchange coefficient

The energy transfer rate between phases is assumed as a function of temperature difference.

$$\dot{Q}_{pq} = h_{pq} (T_p - T_q) \quad (7)$$

where  $h_{pq} = h_{qp}$  is the heat transfer coefficient between  $p$  and  $q$  phases. The heat transfer coefficient is related to the Nusselt number of  $p$  phase ( $Nu_p$ ); in this way,

$$h_{pq} = \frac{6k_q \alpha_p \alpha_q Nu_p}{d_p^2} \quad (8)$$

where  $k_q$  is the thermal conductivity coefficient of q phase. In fluid–fluid multiphase flow mode, the Runz–Marshall equation is used [51],

$$Nu_p = 2.0 + 0.6Re_p^{1/2} Pr \tag{9}$$

where  $Re_p$  is the Reynolds number based on p phase diameter and relative velocity of the two phases  $|\vec{u}_p - \vec{u}_q|$  and Pr is the Prandtl number of q phase,

$$Pr = \frac{c_{pq}\mu_q}{k_q} \tag{10}$$

**Momentum equation**

Momentum equilibrium for the phase q leads to the following equation:

$$\frac{\partial}{\partial t}(\alpha_q \rho_q \vec{v}_q) + \nabla \cdot (\alpha_q \rho_q \vec{v}_q \vec{v}_q) = -\alpha_q \nabla p + \nabla \cdot \bar{\tau}_q + \alpha_q \rho_q \vec{g} + \sum_{p=1}^n (\vec{R}_{pq} + \dot{m}_{pq} \vec{v}_{pq} - \dot{m}_{qp} \vec{v}_{qp}) + (\vec{F}_q + \vec{F}_{lift,q} + \vec{F}_{vm,q}) \tag{11}$$

in which  $\bar{\tau}_q$  is stress–strain tensor of the phase q.

$$\bar{\tau}_q = \alpha_q \mu_q (\nabla \vec{v}_q + \nabla \vec{v}_q^T) + \alpha_q (\lambda_q - \frac{2}{3} \mu_q) \nabla \cdot \vec{v}_q \vec{I} \tag{12}$$

in which  $\mu_q$  and  $\lambda_q$  are, respectively, the dynamic and bulk viscosity of the phase q,  $\vec{F}_q$  is the external volumetric force,  $\vec{F}_{lift,q}$  is the lift force,  $\vec{F}_{vm,q}$  is the virtual mass force,  $\vec{R}_{pq}$  is the force of interactions between phases and p is the common pressure between all phases.

**Interphase force**

Equation (11) is completed with the proper equation for the interphase force  $\vec{R}_{pq}$ . This force depends on the friction, pressure, adhesion and other effects, and in the case where  $\vec{R}_{qp} = \vec{R}_{pq}$  and  $\vec{R}_{pq} = 0$ .

$$\sum_{p=1}^n \vec{R}_{pq} = \sum_{p=1}^n K_{pq} (\vec{v}_p - \vec{v}_q) \tag{13}$$

where  $K_{pq} = K_{qp}$  is the interphase momentum exchange coefficient.

**Virtual mass force**

Inertia of the mass of initial phase is applied to the particle due to an accelerated particle in the form of a virtual mass force,

$$\vec{F}_{vm} = 0.5 \rho_p \alpha_q \left( \frac{d_q \vec{v}_p}{dt} - \frac{d_p \vec{v}_p}{dt} \right) \tag{14}$$

$$\frac{d_q \dots}{dt} = \frac{\partial \dots}{\partial t} + (\vec{v}_q \cdot \nabla) \dots \tag{15}$$

The force of virtual mass  $\vec{F}_{mv}$  will be added to the right side of momentum equation for each of the two phases,

$$(\vec{F}_{mv,q} = -\vec{F}_{mv,p}) \tag{16}$$

**Lift force**

Lift force applied to the secondary phase p in the initial phase q is calculated from the following equation:

$$\vec{F}_{lift} = -0.5 \rho_q \alpha_q (\vec{v}_q - \vec{v}_p) \times (\nabla \times \vec{v}_q) \tag{17}$$

Lift force will be added to the right side of momentum equation for both phases:

$$(\vec{F}_{lift,q} = -\vec{F}_{lift,p}) \tag{18}$$

**Fluid–fluid exchange coefficient**

The coefficient of exchange for these liquid–liquid or gas–liquid bubble mixture types can be written in the following general form,

$$K_{pq} = \frac{\alpha_q \alpha_p \rho_p f}{\tau_p} \tag{19}$$

where  $f$  is the post function and  $\tau_p$  is the particle relaxation time defined as follows:

$$\tau_p = \frac{\rho_p d_p^2}{18 \mu_q} \tag{20}$$

where  $d_p$  is the diameter of the bubbles or drops of the phase p.

**Continuity equation**

The volume fraction of each phase is calculated by continuity equation,

$$\frac{1}{\rho_{rq}} \left( \frac{\partial}{\partial t} (\alpha_q \rho_q) \right) + \nabla \cdot (\alpha_q \rho_q \vec{v}_q) = \sum_{p=1}^n (\dot{m}_{pq} - \dot{m}_{qp}) \tag{21}$$

where  $\rho_{rq}$  is the phase reference density or the average volume density of the phase q in the solution domain.

## The basic equations in RPI boiling model

In this model, the thermal energy transferred from the wall to the fluid is divided into three parts.

$$q_w = q_C + q_Q + q_E \quad (22)$$

The convective heat flux ( $q_c$ ) is obtained from the following equation:

$$q_c = h_c(T_w - T_L)(1 - A_b) \quad (23)$$

in which  $A_b$  is the heated surface of a wall covered with nucleus boiling bubbles and  $(1 - A_b)$  is a region covered by a fluid phase. In this equation,  $h_c$  represents the single-phase heat transfer coefficient,  $T_w$  is the wall temperature and  $T_L$  is the input fluid temperature.

Defective heat flux ( $q_Q$ ) is the average circular energy transfer associated with the wall adjacent film after the separation of the vapor bubbles obtained from the following equation:

$$q_Q = \frac{2k_l}{\sqrt{\pi\lambda_l T}}(T_w - T_l) \quad (24)$$

where  $k_l$  is the thermal conductivity coefficient,  $T$  is the time of alternation and  $\lambda_l$  is the penetration term expressed as follows:

$$\lambda_l = \frac{k_l}{\rho_l c_{pl}} \quad (25)$$

## Evaporative heat flux

Evaporative heat flux ( $q_E$ ) is expressed as follows:

$$q_E = V_d N_w \rho_v h_{fv} f \quad (26)$$

where  $V_d$  represents the volume of vapor bubble,  $N_w$  expresses the nucleus local density,  $\rho_v$  is the vapor density,  $h_{fv}$  is the hidden heat of evaporation and  $f$  is the frequency of the vapor deviation. In the following, some of the parameters mentioned in the above equations are introduced and studied.

## Infiltration area

$$A_b = K \frac{N_w \pi D_w^2}{4} \quad (27)$$

$$A_b = \min\left(1, K \frac{N_w \pi D_w^2}{4}\right) \quad (28)$$

where  $K$  is a constant in the range of 1.8–5, which is generally considered to be 4.

## The frequency of bubble deviation

It is expressed by the following equation:

$$f = \frac{1}{T} = \sqrt{\frac{4g(\rho_l - \rho_v)}{3\rho_l D_w}} \quad (29)$$

## Local nuclear density

$$N_w = C^n (T_w - T_{sat})^n \quad (30)$$

According to the empirical equation of Lemmert and Chawla [52], in the above equation,  $n = 1.88$  and  $c = 210$ .

## Turbulence model

One of the subsets of  $k$ - $\omega$  model that can be used to solve this problem is known as  $k$ - $\omega$  shear stress transfer model in which the ideas of two standard models  $k$ - $\varepsilon$  and  $k$ - $\omega$  are combined. This model considers the following equations for turbulent kinetic energy and special loss rate [52].

## Kinetic energy of turbulence

$$\frac{\partial(\rho\omega)}{\partial t} + \frac{\partial(\rho\omega u_i)}{\partial x_i} \left( \Gamma_\omega \frac{\partial\omega}{\partial x_j} \right) + G_\omega - Y_\omega + S_\omega + D_\omega \quad (31)$$

## Dissipation rate

$$\frac{\partial(\rho k)}{\partial t} + \frac{\partial(\rho k u_i)}{\partial x_i} = \frac{\partial}{\partial x_j} \left( \Gamma_k \frac{\partial k}{\partial x_j} \right) + G_k - Y_k + S_k \quad (32)$$

$G_k$  is the kinetic energy of turbulence generated due to average velocity gradients [53]:

$$G_k = -\rho \overline{u_i' u_j'} \frac{\partial \overline{u_i}}{\partial x_j} \quad (33)$$

$G_\omega$  is the turbulence rate of generated loss [53]:

$$G_\omega = \alpha \frac{\omega}{k} G_k \quad (34)$$

where  $\alpha$  is due to Reynolds lower number corrections.  $D_\omega$  is the intersection diffusion expression, which causes the standard model  $k$ - $\varepsilon$  combined with the standard model  $k$ - $\omega$ .  $S_k$  and  $S_\omega$  are source sentences.  $\Gamma_k$  and  $\Gamma_\omega$  are, respectively, the effective diffusion coefficients of  $k$  and  $\varepsilon$  [53]:

$$\Gamma_k = \mu + \frac{\mu_t}{\sigma_k} \quad (35)$$

$$\Gamma_\omega = \mu + \frac{\mu_t}{\sigma_\omega} \tag{36}$$

where  $\sigma_k$  and  $\sigma_\omega$  are turbulence integer numbers for  $k$  and  $\omega$ , respectively. The turbulence viscosity is calculated as follows [53]:

$$\mu_t = \frac{\rho k}{\omega} \frac{1}{\max\left[\frac{1}{\alpha^*}, \frac{\Omega F_2}{\alpha_1 \omega}\right]} \tag{37}$$

$$\Omega = \sqrt{2\Omega_{ij}\Omega_{ij}} \tag{38}$$

$$\sigma_k = \frac{1}{F_1/\sigma_{k,1} + (1 - F_1)/\sigma_{k,2}} \tag{39}$$

$$\sigma_\omega = \frac{1}{F_1/\sigma_{\omega,1} + (1 - F_1)/\sigma_{\omega,2}} \tag{40}$$

where  $F_1$  and  $F_2$  are mixing functions and their purpose is to make the model function properly in areas close to the wall and away from the wall.  $\Omega_{ij}$  is the mean rotation rate, and  $\alpha^*$  is defined as follows [53]:

$$\alpha^* = \alpha_\infty^* \left( \frac{\alpha_0^* + Re_t/R_k}{1 + Re_t/R_k} \right) \tag{41}$$

where  $Re_t = \frac{\rho k}{\mu \omega}$ ,  $R_k$ ,  $\alpha_\infty^*$  and  $\alpha_0^*$  are the constants of the model. Also, the turbulence intensity and longitudinal scale are obtained by (42) and (43)

$$I = 0.16Re^{-\frac{1}{8}} \tag{42}$$

$$l = 0.07L, (L = D) \tag{43}$$

In this study, based on the geometry of the problem, the turbulence intensity is equal to 3.87% and turbulence longitudinal scale is 0.0035 m. Finally, numerical modeling has been performed using RPI boiling model and considering post forces.

### Problem statement and solution method

#### Geometric model and operating conditions

Since in this problem we have studied the flow in the vertical and diagonal tubes, the effect of gravitational force on the changes in two-phase flow regimes in a vertical direction along the plane is similar to the changes in the radial direction. Therefore, instead of 3D geometry, 2D modeling is used. In this model, we have attempted to make the density of the computational network near the

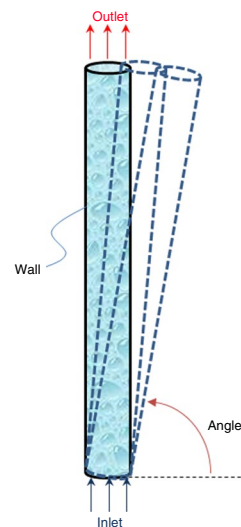
wall higher than the zone near the tube axis so that more accurate calculations can be done near the wall and the model can be better solved. In the given network, we have used rectangular cells with a desirable growth factor in length and diameter; for this reason, these are classified in the group of organized networks. The proposed geometry is a tube with a diameter of 0.025 m and length of 1 m, which, for modeling, to reduce the volume of calculations and the time to reach the final solution, the problem is solved as an axisymmetric problem. Figure 1 shows the computational network of the given problem.

In the fluid flow direction through the tube inlet due to the phase shift of single-phase flow to two-phase flow and the generation of boiling patterns, smaller cells of the network are selected. The network density in these zones needs to be further elaborated in order to accurately model the process of evaporation and flow of fluid entering the two-phase zone. Here, the liquid is introduced into the model with a flow rate of 0.05 kg s<sup>-1</sup> and inside the heat dissipation zone of the wall, which has a constant-temperature range of 0–470 °C above the inlet temperature that is the beginning of the two-phase flow. Water and vapor flows are considered to be incompressible. The boundary conditions applied to each of the sides of the network are indicated in Table 1.

#### Mesh independency

Regarding high-temperature gradients along the tubes, the criterion of downsizing the mesh and examining the convergence of the solution, the first cell layer is considered along the wall, and thus, the cell is broken with a constant relative ratio to the previous generation mesh each time. In order to study the mesh independency, the thermal fluid

Fig. 1 Schematics of the given problem



variables and mean heat transfer coefficient of the tubes have been compared in nine different meshes. The results are shown in Table 2.

Considering the observations on the basis of the slight difference between the flux values between the fifth and sixth mesh, the sixth mesh with the number of 15,000 cells has been used as the accepted mesh in the problem.

### Numerical modeling

A finite volume method has been used to perform the required simulations. The equations are solved using a pressure-based solution. In solving this problem, the boiling model has been used as one of the Eulerian model theory sub-branches. The pressure and velocity equations are solved simultaneously using phase coupled SIMPLE methods. In order to make the equations discrete, the modified HRIC method is used for the volume fractional equation, and for the other equations, second-order approximation is used. Also, sub-discount coefficients have been considered for solving the equations of pressure, momentum, volume fraction, turbulence and energy variables as 0.3, 0.5, 0.5, 0.8 and 0.1, respectively. Also, for solving a problem under different conditions, the time step has been used in the range of 0.01–0.00001. In order to move the solution in a path toward mass equilibrium with a mass balance error of about 0.04 of a variable in

the input, we have attempted to use smaller time steps in order to perform numerical modeling in a desirable manner. In order to solve this problem, a system with 7 nucleolus 2 GHz processor and 12 gigabytes memory has been used.

### Dimensionless quantities

$$\text{Dimensionless position} = \frac{x}{l} \tag{44}$$

where  $x$  is the distance from the beginning of the tube and  $l$  is the tube length.

$$\text{Dimensionless axial velocity} = \frac{V}{U} \tag{45}$$

where  $V$  is the velocity of the fluid phase and  $U$  is the flow velocity at the inlet.

$$U = \frac{\dot{m}}{\rho \cdot A} \tag{46}$$

where  $\dot{m}$  is the mass ratio of the inlet.

$$\text{Dimensionless tube diameter} = \frac{d_y}{1/D} \tag{47}$$

where  $d_y$  is the diameter of the tube axis and  $D$  is the diameter of the tube.

### Validation

In order to validate the present problem, we utilized the laboratory data used by Johansen [54]. As shown in Fig. 2, the change in the convective heat transfer coefficient due to the numerical solution results had a similar process to the results of the Johansen data. This difference shows the accuracy of numerical solution method used in the present problem. However, the error shown in this figure is inevitably due to factors such as networking of the model, its solution method,

**Table 1** The boundary conditions applied to issue

Conditions	Boundary condition
Mass flow rate = 0.05 kg s <sup>-1</sup> Steam flow rate = 0 kg s <sup>-1</sup> Temperature = $T_{\text{sat}} = 373.15$ K	Inlet terms
Wall temperature = constant	Wall condition
Temperature = $T_{\text{sat}}$	Outlet term

**Table 2** Results obtained in order to achieve the independence of the computational network

Network number	Number of longitudinal meshes	Number of transverse meshes	Total number of meshes	Heat flux/W m <sup>-2</sup>
1	300	15	4500	12,048
2	400	15	6000	14,015
3	500	15	7500	15,408
4	600	15	9000	15,614
5	600	25	15,000	15,745
6	600	35	21,000	15,876

as well as other factors affecting the solution. This error, with the descending process, finally reaches its maximum, which is approximately 14%.

## Results and discussion

### The effect of changes in the wall temperature on the boiling zone of saturation (two phases)

As mentioned earlier, the flow of water in the form of a saturated and single-phase liquid enters a tube at different angles and in the opposite direction of gravity of the earth in an upward direction. By applying a constant-temperature

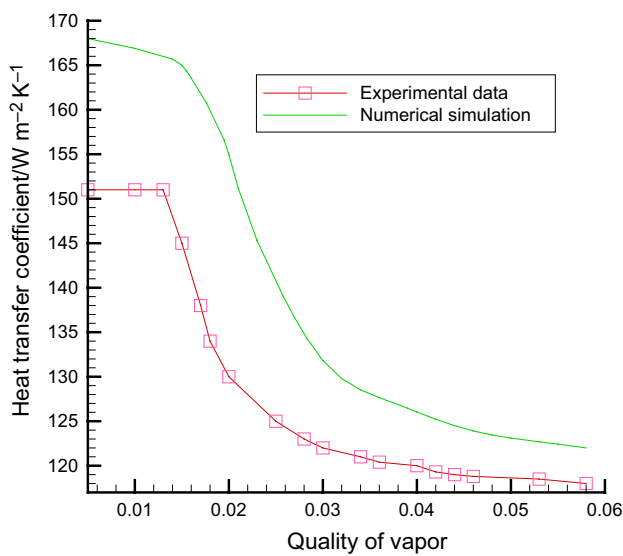


Fig. 2 Comparison of numerical solution with Johansen laboratory data [54]

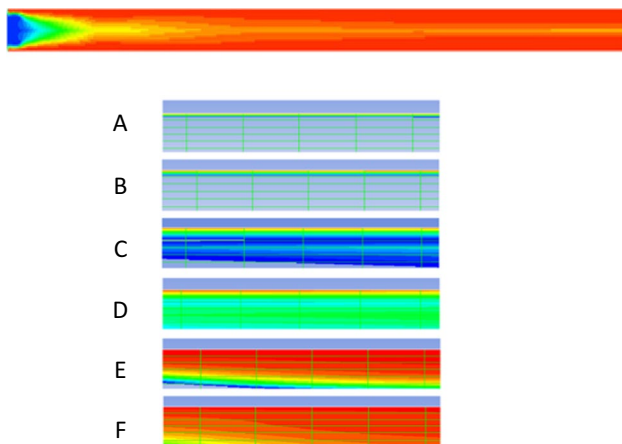


Fig. 3 The effect of changes in the wall temperature on the thickness of the vapor phase next to the wall (A=10 °C, B=30 °C, C=100 °C, D=135 °C, E=260 °C, F=270 °C)

difference to the wall, the liquid phase begins to vapor and causes the formation of two-phase flows. Figure 3 shows the effect of changing the difference between the average wall temperature on the boiling region of saturation and thickness of the vapor phase on the wall due to the application of different temperatures to the surface in the tube element.

As shown in Fig. 3, in all angles, with the application of a temperature higher than the saturation liquid temperature into the wall, fine vapor bubbles form on the wall. With increasing the difference between the temperatures of the wall and fluid, the process of formation and growth of the bubbles increases and the volume fraction of the vapor phase increases on the wall. Further, this increase in the temperature difference causes an increase in the temperature of the fluid mass, which itself generates two-phase regime patterns along less length from the beginning of the pipe. With increasing the difference between the wall and fluid temperature, the film diameter of the vapor phase film is increased on the wall.

Figures 4 and 5 show the effect of changing the temperature difference between the wall and inlet fluid on the boiling region of saturation (two phases) and the corresponding vapor-phase contours until the temperature reaches the critical heat flux in a sequential manner and according to all three angles.

As shown in Fig. 4 related to vapor-phase contours, with applying a temperature higher than the saturation fluid temperature vapor bubbles formed on the wall in the inlet. With increasing the difference in the temperature of the wall and fluid, also the process of formation and growth of bubbles increases, and the volume fraction of the vapor phase increases in the wall. Because the inlet temperature faster reached higher temperatures than saturation, and mass transfer occurs from the liquid to the vapor phase. Of course, the transfer of mass from the liquid phase to the vapor phase begins as it is shown in the figure from the very beginning of the tube. In fact, this increase occurs in the temperature difference between the wall and fluid, which increases the energy received by each computing cell located near the wall, and then, this increase in temperature difference leads to an increase in fluid mass temperature, which itself forms the patterns of the two-phase regime in less length from the beginning of the tube. However, one cannot ignore the fact that the increase in the volume fraction of the vapor phase is proportional to the increase in the average temperature difference of the wall to its highest value, before the occurrence of critical heat flux (at the temperature of 203 °C), and then another similar process with an increasing process before the occurrence of critical heat flux cannot be expected. After the occurrence of critical heat flux, with the continued increase in the temperature difference between the wall and inlet fluid, the volume fraction reduced because when the bubbles separating from the surface are equal to the produced

bubbles heat transfer reaches its highest point, where critical heat flux occurs, after which other bubbles will not be able to separate from the interface, and therefore the diameter of the liquid film will increase.

As shown in Fig. 5, at 85 °C to the temperature difference of 300 °C, the volume fraction increased and subsequently reduced, which had the same cause as at an angle 80°.

As shown in Fig. 6, at a 90° angle, with increasing the temperature difference between the wall and inlet fluid up to 270 °C, the thickness of the vapor layer in the wall increased, and then, after the occurrence of critical heat flux, with the continuation of the increase in the average wall temperature difference, the volume fraction reduced, and as shown in Figs. 3–5, with increasing the tube slope the temperature with the highest volume fraction of nanoparticles is reduced. The reason for this reduction in the temperature is that the increase in the positive slope of the tube leads to faster growth of the instability and a faster change in the layer flow regime into the flow regime of the slug.

### The effect of changing the wall temperature difference and inlet fluid on volume fraction of the vapor

As it is seen in the previous section, it is more correct to divide the results of each section into two regions, one related to the results before the occurrence of critical heat flux and another related to the results after the occurrence of critical heat flux. In this section, at all angles, the process of changing the values of the average volume fraction of the outlet vapor by the change in the average temperature difference between the wall and fluid is shown in tables, and then, the process of changes in the volume fraction of the outlet vapor in the tube axis with advance in the tube length is provided with the relevant figures. Tables 3–5 show the effect of increasing the temperature difference on values of volume fraction of the vapor phase at various angles.

As shown in Table 3, the increase in the wall and fluid temperature difference increases the heat transfer to the liquid and the molecular movement, resulting in the breakdown of the intermolecular fluid links and the conversion of the liquid phase to vapor phase, so this increasing process of volume fraction of the vapor has reached a temperature difference of 320 °C to its extreme limit among other differences in the temperatures studied. At the temperature 330 °C, which is related to the zone after the occurrence of critical heat flux, the process changed from ascending to descending. The reason for this is that the bubbles of the surface are equalized with bubbles produced, and the bubbles will no longer be able to separate from the interface, and the volume fraction of the vapor reduced. Figures 4–6 show the effect of increasing the wall temperature on the vapor volume fraction at an angle of 80°.

As shown in Fig. 7, the process of changing vapor volume fraction to reaching the critical heat flux and after it with increasing the temperature difference between the wall and inlet fluid the volume fraction of the vapor increased along the initial tube length, and this process continues until the temperature difference of 320 °C, where critical heat flux occurs and had the highest value, and then, with the continuous increase in temperature, vapor volume fraction reduced. It is also found that in lower heat flux, the length of zones that include zero vapor volume fraction (the same saturated fluid zone) is greater and gradually reduced with increasing heat flux. The flow enters the two-phase zone. The reason for this is that increasing the temperature difference increases the energy received by the fluid molecules as well as more energy is absorbed to break the intermolecular bonds, and vapor volume fraction increased. As shown in Fig. 7, an increase in the volume fraction in the beginning of the tube is very fast because the temperature of the inlet fluid is more than the saturation temperature, and the mass transfer occurs from liquid to vapor, which is actually an increase in the wall temperature, which increases the energy received by any computing cell that is near the wall.

As shown in Table 4, at an 85° angle, this process has reached its maximum at a temperature difference of 300 °C among other temperature differences studied and the reason is similar to the explanation given for an angle of 80°. Figure 8 shows the effect of increasing the wall temperature on vapor volume fraction at an 85° angle.

As shown in Fig. 8, vapor volume fraction increases with increasing the wall temperature difference up to a temperature difference of 300 °C, where critical heat flux occurs and has the highest value, and reduced after critical heat flux, with the continuation of the increase in the average wall temperature difference, and the increase in outlet vapor volume fraction at the very beginning of the tube length is very fast, and the reasons for this change in vapor volume fraction are similar to those described for the angle 80°.

As shown in Table 5, at a 90° angle, this process has reached its maximum at a temperature difference of around 280° C among other temperature differences studied, and compared to Tables 3 and 4, it is observed that with increasing the tube angle, the higher volume fraction of vapor phase occurs at a lower temperature due to the rapid changes in the flow pattern due to increased slope and faster phase conversion from liquid to vapor. Figure 9 shows the effect of increasing the wall temperature on the vapor volume fraction at a 90° angle.

As shown in Fig. 9, at a 90° angle, with increasing the temperature difference between the wall and inlet fluid, vapor volume fraction increased, and this process of increasing the volume fraction begins at the beginning of the tube length; comparing with Figs. 7 and 8, it is found that with



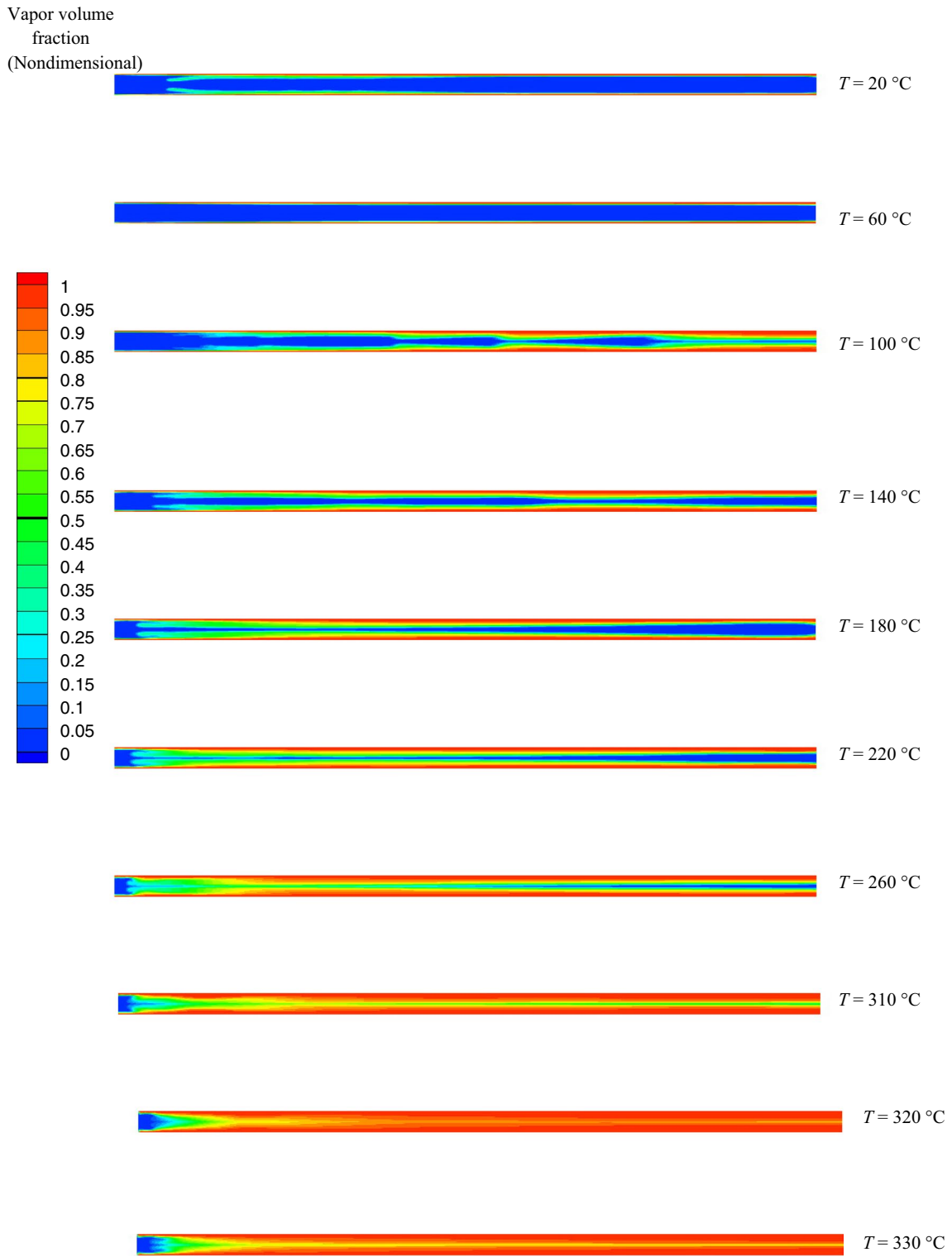


**Fig. 4** The effect of changing the temperature difference between the wall and inlet fluid on the boiling region of saturation and the vapor-phase contours at angle  $80\text{ }^{\circ}\text{C}$

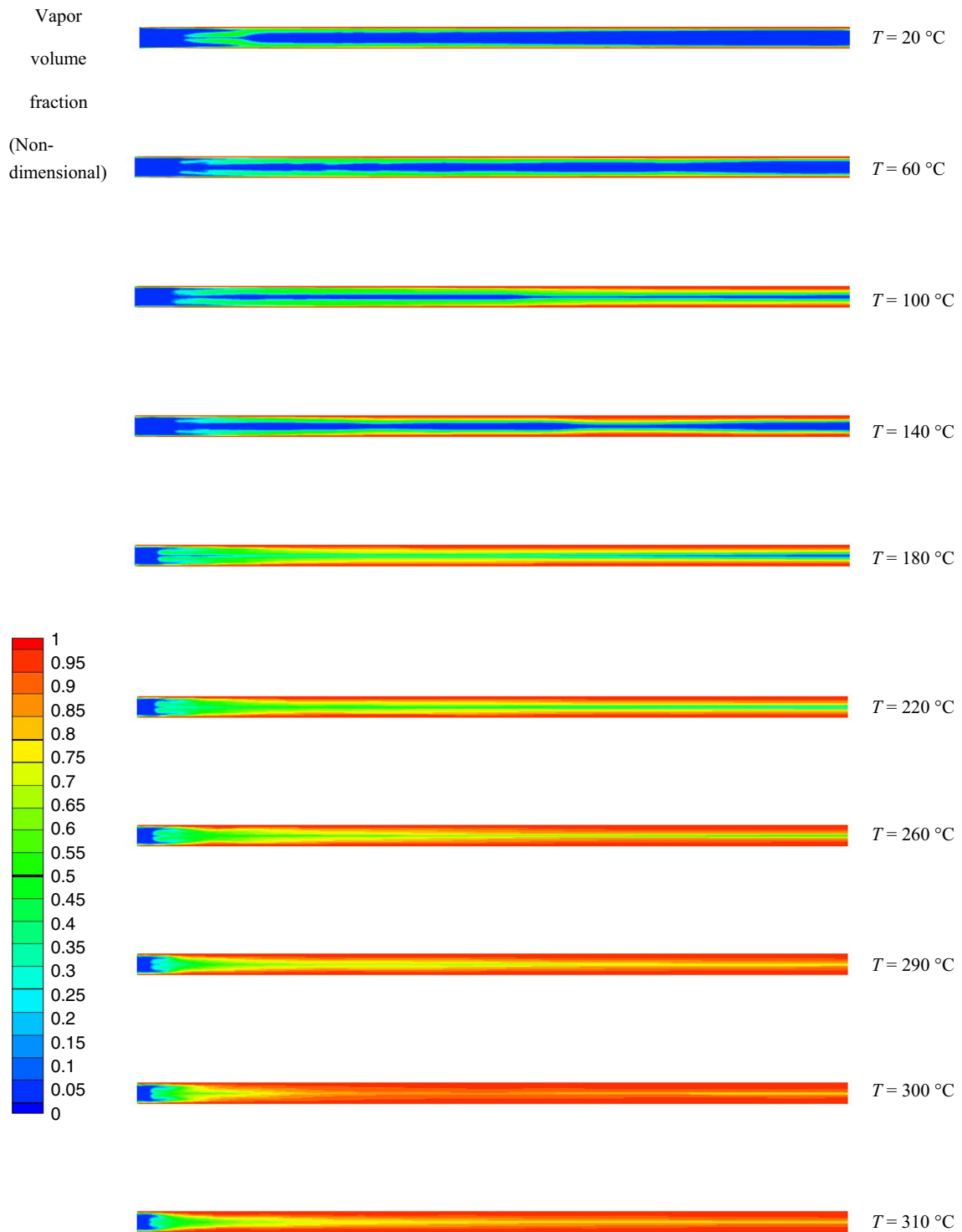


**Fig. 5** The effect of changing the temperature difference between the wall and inlet fluid on the boiling region of saturation and the vapor-phase contours at angle  $85\text{ }^{\circ}\text{C}$

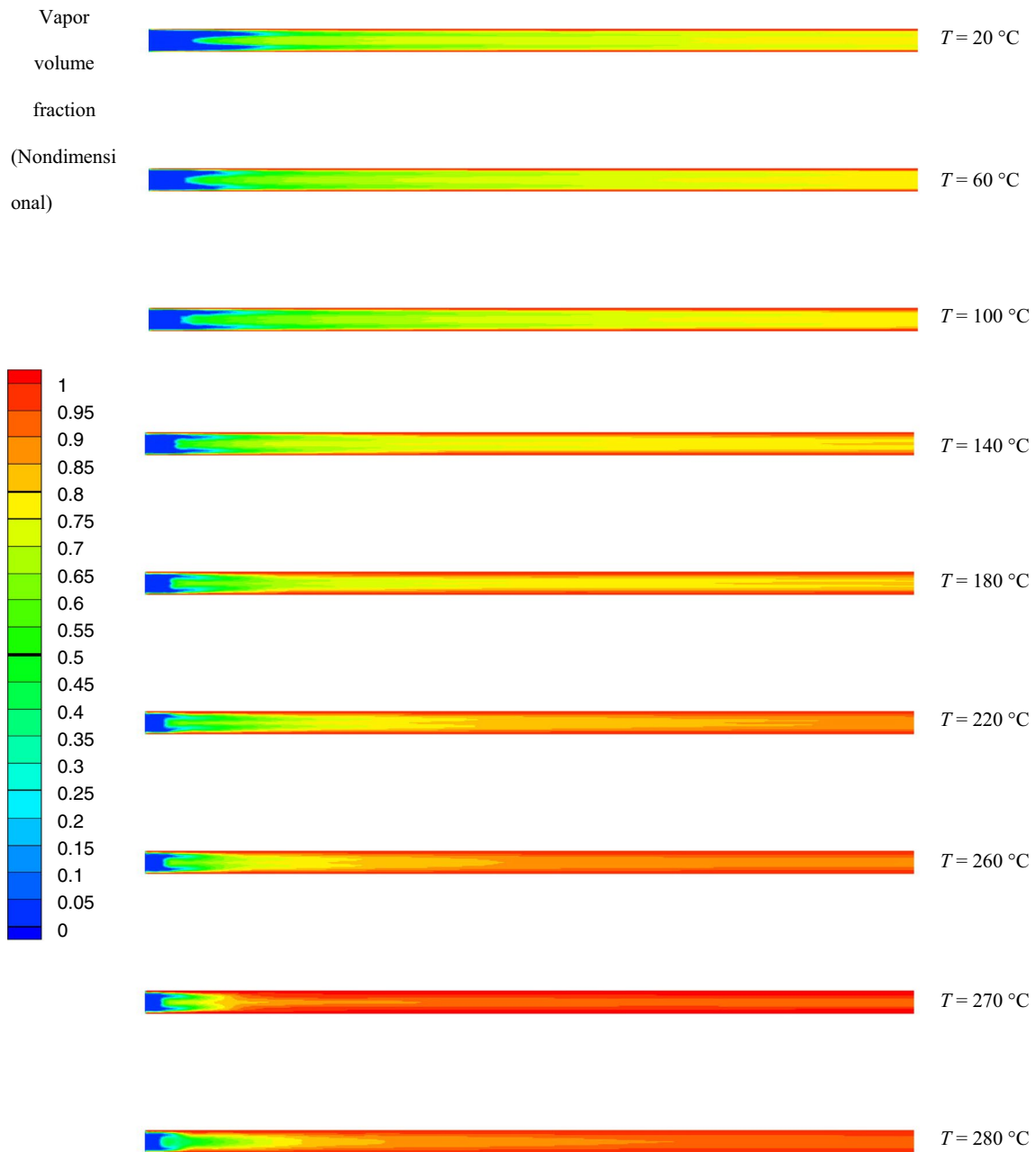


**Fig. 6** The effect of changing the temperature difference between the wall and inlet fluid on the boiling region of saturation and the vapor-phase contours at angle 90 °C

increasing the tube angle at all temperatures studied, vapor volume fraction is higher, due to the faster growth of instability due to increased slope of the tube. These results are consistent with the results of Andreussi and Persen [54].

**The effect of changes in the wall average temperature on the heat flux**

One of the main objectives of this study is to study the effects of changing the average temperature difference

between the wall and fluid on changes in heat flux at various angles, which finally will lead to the achievement of critical heat flux at these angles. The question now is whether the process of changes in the flux in the whole process will be the same or will change after the occurrence of critical heat flux. In principle, it can be said that an increase in the average temperature difference between the wall and fluid is directly related to the increase in the heat flux. As the temperature difference increases, the flux increases, although this flux increase continues to the point where the critical

**Table 3** The effect of change in the average temperature of the wall on the values of the average volume fraction of the outlet vapor at angle 80 °C

Temperature difference value between the wall and fluid/°C	Values of the average volume fraction of the outlet vapor
260	0.84
280	0.92
300	0.94
310	0.95
320	0.97
330	0.96

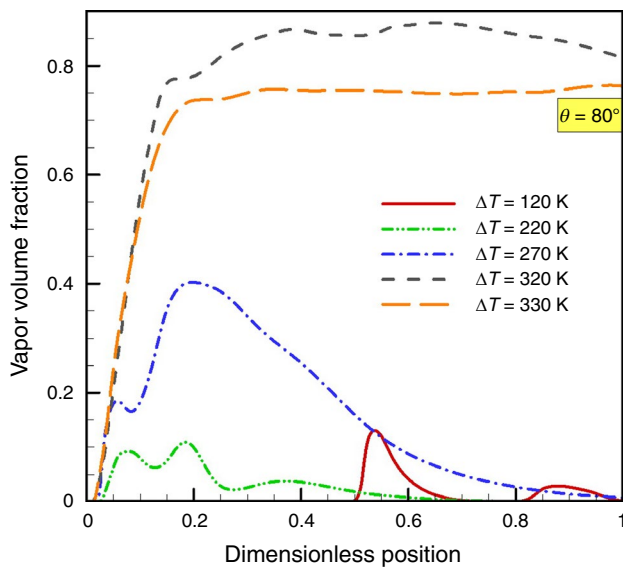


**Fig. 7** The effect of changing temperature difference between the wall and inlet fluid on volume fraction of the vapor at angle 80 °C

**Table 4** The effect of change in the average temperature of the wall on the values of the average volume fraction of the outlet vapor at angle 85 °C

Temperature difference value between the wall and fluid/°C	the values of the average volume fraction of the outlet vapor
240	0.86
260	0.94
280	0.95
290	0.96
300	0.97
310	0.96

heat flux occurs. Since then, with increasing the wall average temperature difference, the heat flux begins to reduce. Increasing the temperature difference and reducing the critical heat flux will mean a sharp reduction in the heat transfer coefficient. In this section, as in the previous section, first

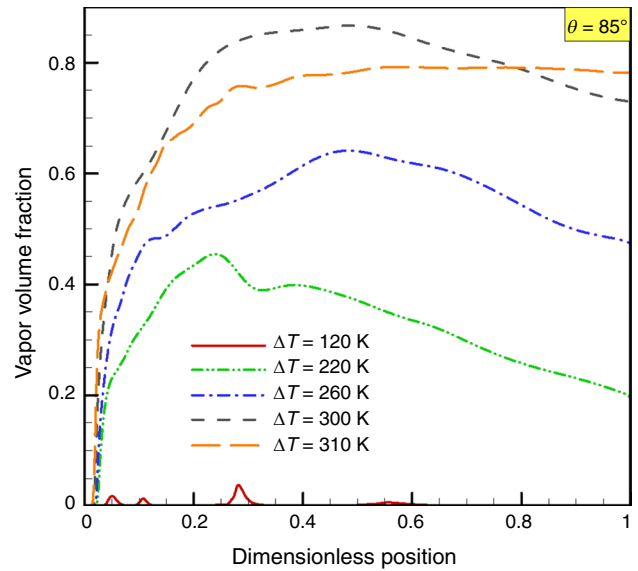


**Fig. 8** The effect of changing temperature difference between the wall and inlet fluid on volume fraction of the vapor at angle 85 °C

**Table 5** The effect of change in the average temperature of the wall on the values of the average volume fraction of the outlet vapor at angle 90 °C

Temperature difference value between the wall and fluid/°C	the values of the average volume fraction of the outlet vapor
240	0.92
250	0.94
260	0.95
270	0.95
280	0.96
300	0.96

we address the effect of increasing the average temperature difference between the wall and fluid on the values of heat flux and then the process of changing the heat flux along the tube length on the wall. Tables 6–8 show the values of the fluxes with increasing the wall average temperature difference at the angles studied.

As shown in Table 6, the heat flux increases with increasing average wall temperature difference up to 320 °C (where critical heat flux occurs) and then reduced which is due to reduced heat transfer coefficient. Figure 10 shows the heat flux in terms of the dimensionless distance at various temperatures at an angle of 80°.

As shown in Fig. 10, the temperature values increase with increasing the average temperature difference between the wall and fluid up to a temperature difference of 320 °C and then again will show a behavior that is completely different from before the occurrence of critical heat flux, as well as at

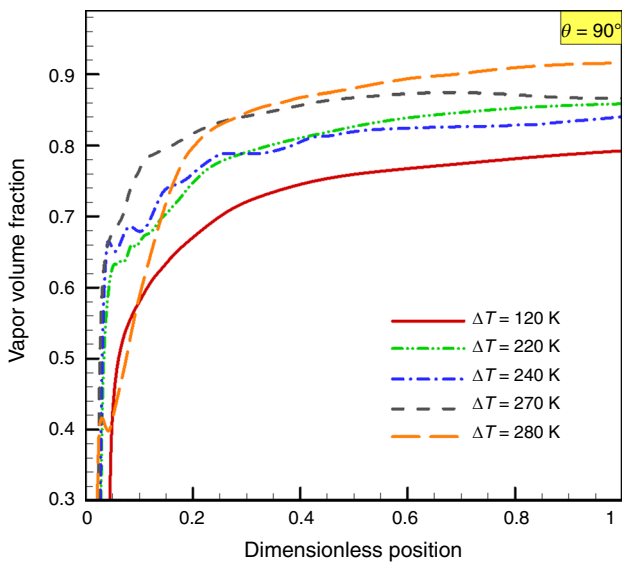


**Fig. 9** The effect of changing temperature difference between the wall and inlet fluid on volume fraction of the vapor at angle 90 °C

320 °C fluctuations of heat flux, especially at the beginning increase, and non-uniform behavior is seen in the figure. The reason for this is similar to the reasons mentioned above for increasing vapor volume fraction in the previous discussion. The increase in the average temperature difference between the wall and fluid is directly related to the increase in the heat flux. As the temperature difference increases, the flux increases as well, but this flux increase continues to reach the critical heat flux; since then, with increasing average wall temperature difference heat flux begins to reduce. Increasing the temperature difference and reducing the critical heat flux will mean a sharp reduction in the heat transfer coefficient. The fluctuations of the heat flux at the beginning of the tube are due to the faster increase in the inlet fluid temperature to higher temperatures than the saturation, rapid changes in the flow pattern and the conversion of the liquid phase and the vapor phase to each other. The formation of the vapor

**Table 6** The effect of temperature difference value between the wall and fluid on the heat flux at angle 80 °C

Temperature difference value between the wall and fluid/°C	wall heat flux/W m <sup>-2</sup>
260	21,111
280	22,365
300	23,814
310	28,856
315	30,322
320	32,142
325	30,614
330	29,966

phase and the uncertain and unpredictable behavior of the vapor formed on the surface, as well as rapid changes in the properties of the vapor, especially the thermal conductivity coefficient, cause fluctuations and instability in the vapor volume fraction curve.

As shown in Table 7, the heat flux increases with increasing average temperature difference between the wall and fluid up to 320 °C (where critical heat flux occurs) and then reduced. Figure 11 shows the process of changing the heat flux in terms of the dimensionless distance at different temperatures at an 85° angle.

In Fig. 11, the same as Fig. 10, the heat flux values have increased with increasing average temperature difference between the wall and fluid, as well as at the temperature 300 °C, fluctuations in heat flux increased, showed a non-uniform behavior where critical heat flux occurs and then again showed a completely different behavior before the occurrence of critical heat flux, and compared with Fig. 10, the temperature of the occurrence of critical heat flux became lower. Also, at this angle, heat flux fluctuations increased compared to the 80° angle due to the increased slope of the tube, resulting in faster growth of instability and a faster change in the flow regime. As shown in Table 8, heat flux increases with an increase in average temperature difference between the wall and fluid up to a temperature difference of 270 °C and reduced after the occurrence of critical heat flux.

As shown in Fig. 12, at a 90° angle, with increasing the temperature difference between the wall and fluid, the heat flux values increase, and after the temperature of 270 °C (where critical heat flux occurs), the heat flux reduced, and as shown in Figs. 10–11, with increasing the slope of the tube, the fluctuations of heat flux and non-uniform behavior of heat flux increased. The reason is that increased slope is

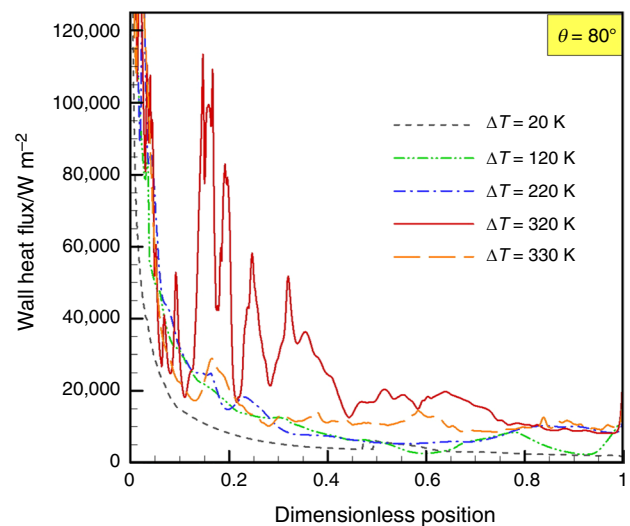


**Fig. 10** The heat flux in terms of the dimensionless distance at various temperatures at an angle of 80°

**Table 7** The effect of temperature difference value between the wall and fluid on the heat flux at angle 85 °C

Temperature difference value between the wall and fluid/°C	heat flux/W m <sup>-2</sup>
240	19,699
260	20,745
280	28,120
290	24,576
295	30,585
300	32,060
305	30,062
310	28,096

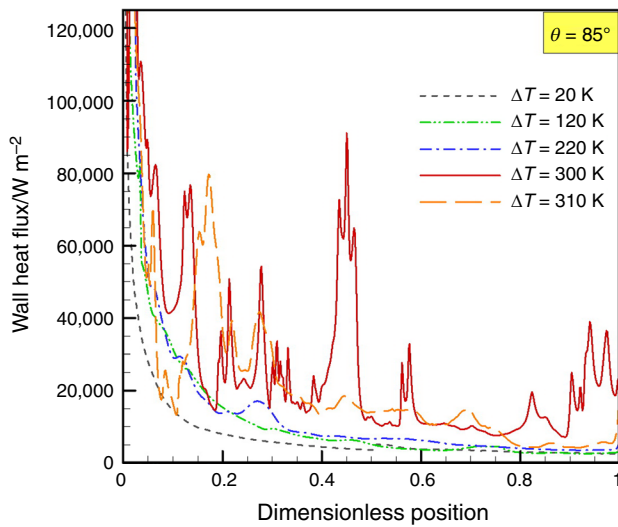


**Fig. 11** The heat flux in terms of the dimensionless distance at various temperatures at an angle of 85°

**Table 8** The effect of temperature difference value between the wall and fluid on the heat flux at angle 90 °C

Temperature difference value between the wall and fluid/°C	Heat flux/W m <sup>-2</sup>
220	20,808
240	22,252
250	24,210
260	24,553
265	30,072
270	38,910
275	30,436
280	32,786

due to the greater effect of gravitational force, resulting in increased recurring flow and a sharp increase in the size of the zone with the flow pattern, as well as an increase in the

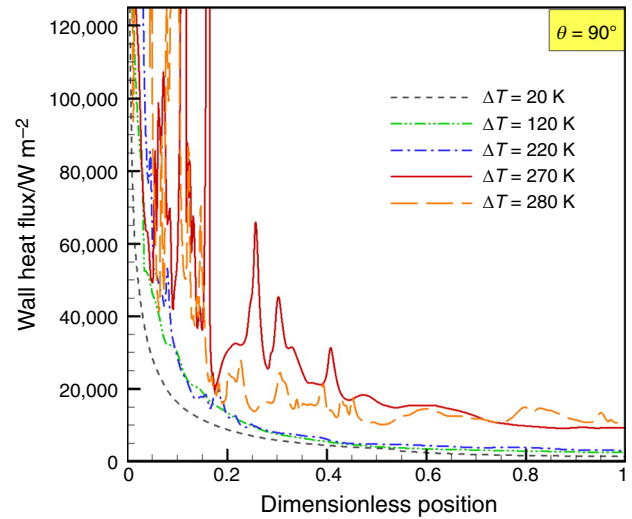


**Fig. 12** The heat flux in terms of the dimensionless distance at various temperatures at an angle of 90°

composition of the two phases, which allows the emergence of a turbulent flow pattern faster.

### The effect of changes in the wall temperature on convective heat transfer coefficient

In this section, another objective of this study is presented that is to find out changes in heat transfer coefficient due to changes in the average wall temperature. Figures 13–15 show the change in the coefficient of heat transfer in terms of dimensionless distance at different temperatures.

As shown in Fig. 13, with increasing the wall temperature, convective heat transfer coefficient reduced, and at the temperature 320 °C, fluctuations and non-uniform behavior of heat transfer coefficient increased. Also, in the initial lengths of the tube, the convective heat transfer coefficient is high and once or at least twice larger than its values in the end lengths of the process. This zone is the same as the zone filled with the saturated liquid phase, and if a bubble of vapor may also be formed, it becomes a liquid phase due to the lack of energy necessary to reach the end parts of the process. In this zone of the flow, because the thermal conductivity of the liquid phase is several times higher than the thermal conductivity of the vapor phase, the heat convective heat transfer coefficient is higher than the other flow zones. With increasing the average wall temperature, the volume fraction of the vapor phase and the mass conversion from the liquid phase to the vapor phase increase, and in contrast, a reduction will be observed in the convective heat transfer coefficient. The reason is that with increasing the volume fraction of the vapor phase, since the vapor phase has a lower thermal conductivity than the liquid phase, the convective heat transfer coefficient is reducing. Now, it should

be verified that, after the occurrence of critical heat flux, with increasing the average wall temperature, the convective heat transfer coefficient of the wall is changed. If the bubbles leave the interface, they increase the mixing and the heat transfer rate increases. When the amount of bubbles that are separated from the surface is equal to the amount of produced bubbles, at this time, the heat transfer reaches its highest level where critical heat flux occurs. These results show a similar process compared to the Gorji study [55]. Figure 14 shows the convective heat transfer coefficient in terms of the dimensionless distance at an 85° angle.

As shown in Fig. 14, with increasing the temperature difference between the wall and inlet fluid, the heat convective heat transfer coefficient reduced. At the temperature of 300 °C, the increase in the heat transfer coefficient fluctuations is observed, as well as these fluctuations are more at the beginning of the tube. With increasing the heat flux of the wall, the unpredictable fluctuations and changes in the heat transfer coefficient curve clearly increase. These changes are generally seen in the zones of the vapor phase, and the main reason is the complex behavior of the two-phase flow, especially the vapor phase on the wall surface. Thus, the formation of the vapor phase on the wall surface and its undetectable behavior makes it impossible to separate the location of liquid and vapor phases with certainty. In other words, the rapid changes in thermo-physical properties between the liquid and vapor phases are the main reason for the fluctuations of the convective heat transfer coefficient of the wall.

As shown in Fig. 15, with increasing the temperature difference between the wall and fluid, the heat convective heat transfer coefficients reduced, and at the temperature 270 °C,

an increase is observed in the heat transfer coefficient fluctuations, and the reasons are similar to the reasons given in the previous two figures.

Figure 16 shows the process of heat flux changes with increasing the temperature difference between the wall and inlet fluid in terms of the dimensionless distance, as well as the process of changes in the heat convective heat transfer coefficient with increasing the wall temperature in terms of a dimensionless distance in three different slopes for better observation and comparison. Also, as shown in the figure, with increasing the temperature difference between the wall

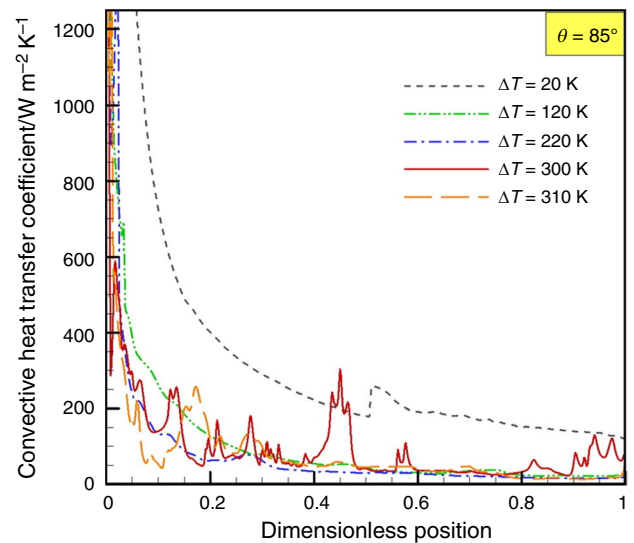


Fig. 14 Convective heat transfer coefficient in terms of dimensionless distance at an angle of 85°

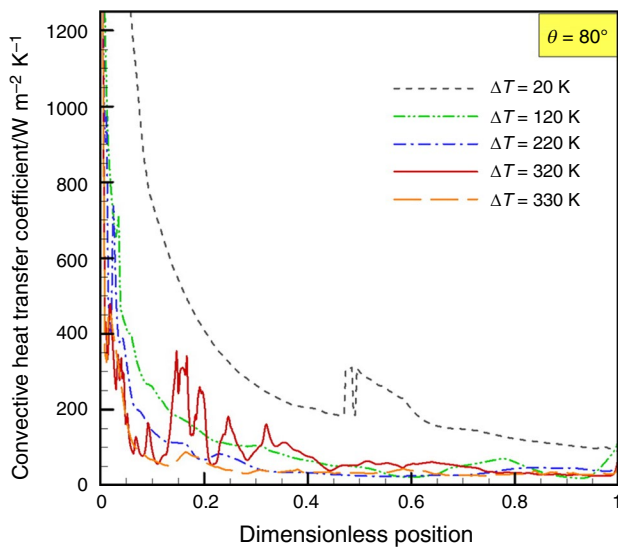


Fig. 13 Convective heat transfer coefficient in terms of dimensionless distance at an angle of 80°

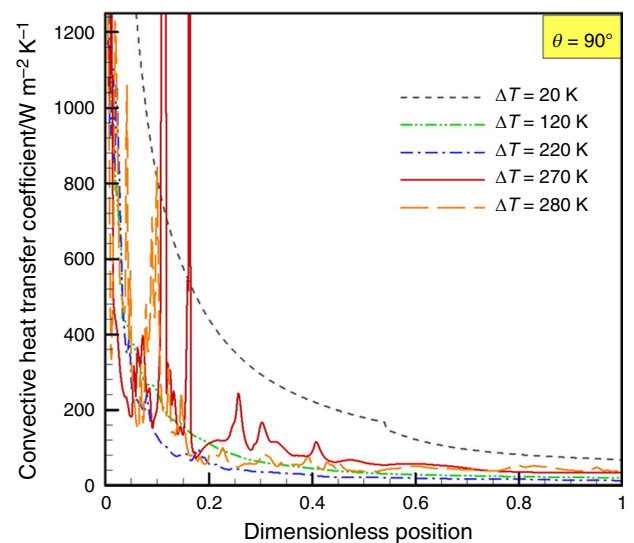
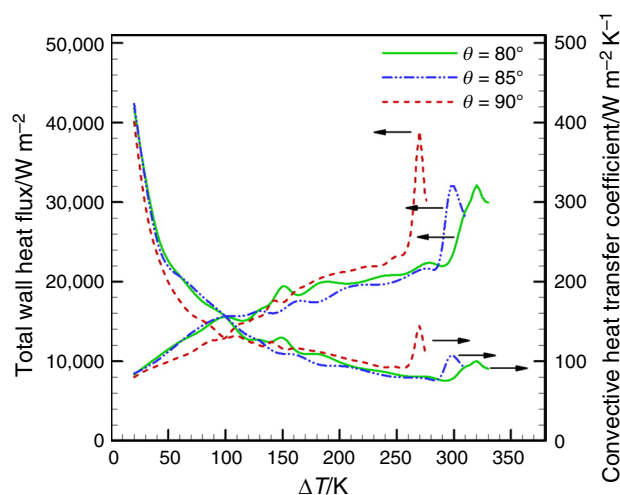


Fig. 15 Convective heat transfer coefficient in terms of dimensionless distance at an angle of 90°

and inlet fluid, heat flux increased and then again a behavior completely different from before the occurrence of critical heat flux will be observed, and with increasing the tube slope the temperature in which the critical heat flux occurs is reduced as well as with increasing the temperature difference between the wall and inlet fluid, the heat convective heat transfer coefficient reduced. The reasons for this behavior of heat flux and heat transfer coefficient are described in the previous sections.

### The effect of changes in the wall temperature on flow velocity

In this section, the process of changes in flow velocity during the process with the progression along the tube at all angles has been studied with increasing the temperature difference between the wall and fluid. With increasing the wall average temperature difference and consequently increasing the transfer energy to the computational cells, the volume fraction of the vapor phase increases, the conversion of mass from the liquid phase to the vapor phase increases and, on the other hand, because the nature of the flow is a fluid in the tube in the upward direction and in the opposite direction of gravity. Bubble particles play a fundamental role in the shape of the velocity profile in these flow regimes, which means that since the particles of the vapor bubbles formed on the wall or the vapor phase have a lower density than the liquid phase, they have a higher velocity. The increase in the average temperature difference between the wall and fluid increases the velocity of the flow pattern and the formation of the vapor bubbles; for this reason, at all angles studied, with increasing the temperature difference between the wall and input fluid, the velocity profiles are larger. Figures 17–20 show changes in the velocity of the flow on the



**Fig. 16** Heat flux and heat transfer coefficient in terms of dimensionless distance

diameter in terms of the dimensionless distances at different temperatures at an angle of  $80^\circ$ .

As shown in Fig. 17, with increasing the distance from the beginning of the tube, the profile of the velocity is greater, as well as the difference in velocity near the wall and tube center is due to increased temperature difference between the wall and inlet fluid near the wall of the vapor-phase mass that is greater than the tube center, and the vapor phase is faster due to its low density; accordingly, it is expected that with increasing the temperature due to further conversion of liquid phase to vapor velocity profiles will have higher values.

As shown in Fig. 18, the profile of the velocity increases up to the end of the tube and shows a higher value than the previous one, and the reason is the same as the description given in the previous one.

As shown in Fig. 19, the velocity profile increases along the tube, and the velocity values along the whole length of the tube show a higher increase compared to the previous one.

As shown in Fig. 20, the velocity is increased at lower temperatures (Figs. 17–19), as well as a slight difference between the velocity in the wall and center in this shape is observed and the profile of the velocity increases to the end of the tube. The reason for the increase in velocity in this case is that here the applied temperature difference to the wall is higher, and this increase in the temperature difference causes an increase in the temperature of the mass of the fluid, resulting in an increase in the volume fraction of the vapor relative to the three previous states, and since bubble particles have a lower density, they show higher velocity.

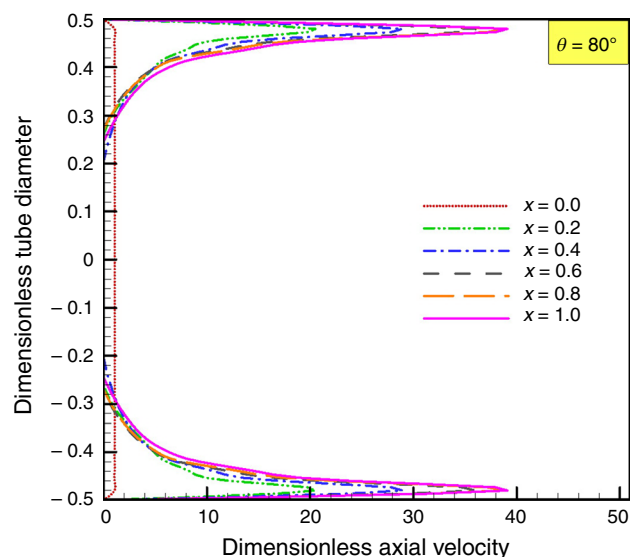


**Fig. 17** Changes in the velocity of the flow over the diameter in terms of the dimensionless distances at temperature difference of  $20^\circ\text{C}$  and  $80^\circ$  angle



Figures 21–24 show changes in the velocity of the flow on the diameter in terms of the dimensionless distances at different temperatures and an angle of 85°.

Figure 21 shows the velocity profile increases along the tube, and the velocity difference is observed near the wall and center, and the reasons are similar to the description given in the previous one.

Figure 23 shows the velocity profile increases up to the end of the tube and higher values.

Figures 21–24 show that with increasing the wall temperature at this angle, the velocity profile increases, and by comparing the changes' process, it is observed that the velocity difference reduced in the tube wall and center with increasing the temperature and at all temperatures the profile of the velocity increases to the end of the tube.

Figures 25–28 show the velocity on the diameter in terms of the dimensionless distances at an angle of 85°.

As shown in Figs. 24–27, with increasing the temperature difference between the wall and inlet fluid at this angle, the velocity magnitude increases, and by comparing the velocity changes in each temperature to the temperature before it is found that as the temperature increases, the difference in velocity reduced in the wall and in the center of the tube, and at all temperatures the velocity profile increased to the end of the tube, and the reasons are similar to the description given for the previous figures.

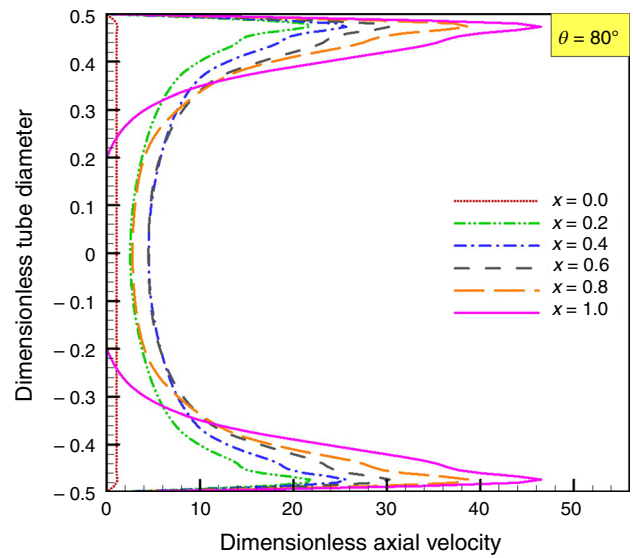


Fig. 19 Changes in the velocity of the flow over the diameter in terms of the dimensionless distances at temperature difference of 220 °C and 80° angle

### The effect of changing the average temperature of the wall on heat flux in different Reynolds numbers

Another objective of this study is to conclude that in different Reynolds numbers, the behavior of heat flux will be varied. For this purpose, only the mass flow rate of the inlet fluid has been changed by holding the fluid constant. The

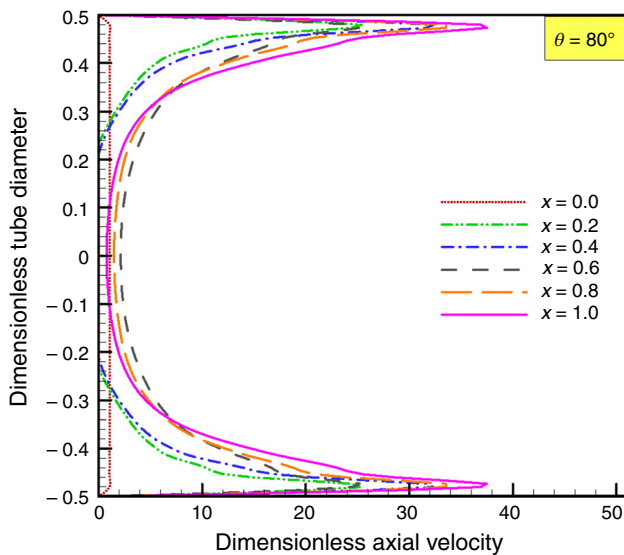


Fig. 18 Changes in the velocity of the flow over the diameter in terms of the dimensionless distances at temperature difference of 120 °C and 80° angle

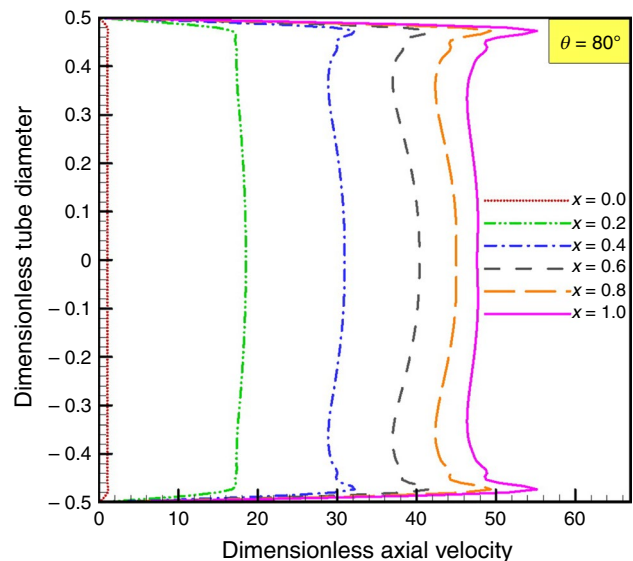
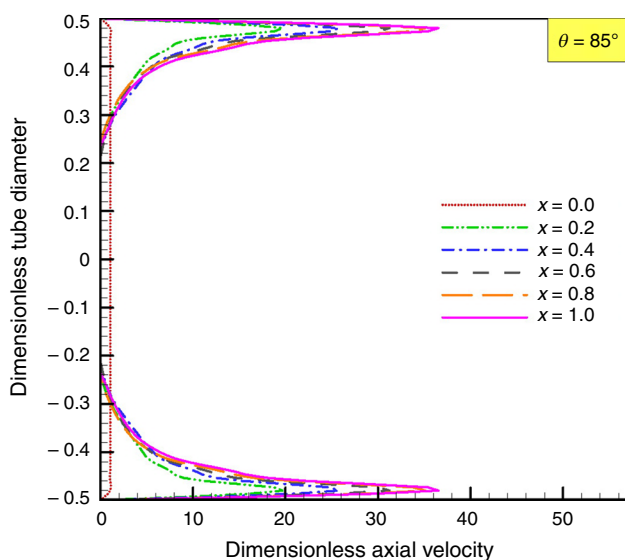
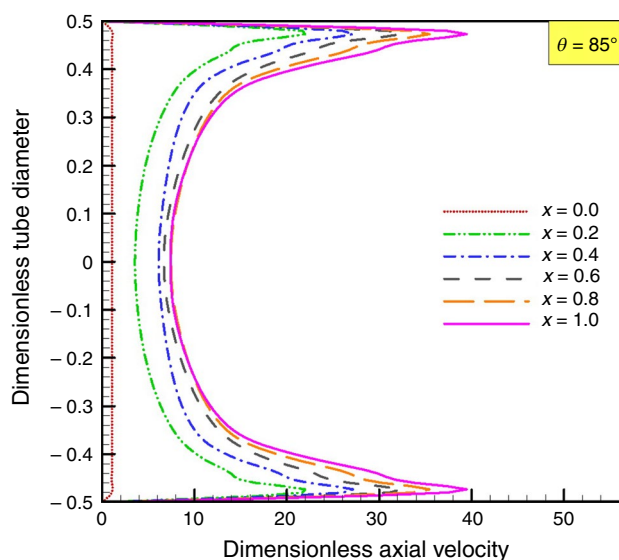


Fig. 20 Changes in the velocity of the flow over the diameter in terms of the dimensionless distances at temperature difference of 320 °C and 80° angle



**Fig. 21** Changes in the velocity of the flow over the diameter in terms of the dimensionless distances at temperature difference of 20 °C and 85° angle



**Fig. 23** Changes in the velocity of the flow over the diameter in terms of the dimensionless distances at temperature difference of 220 °C and 85° angle

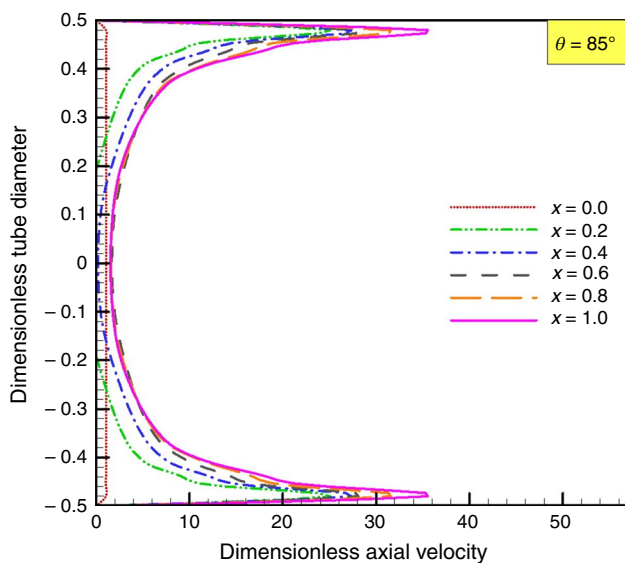


**Fig. 22** Changes in the velocity of the flow over the diameter in terms of the dimensionless distances at temperature difference of 120 °C and 85° angle

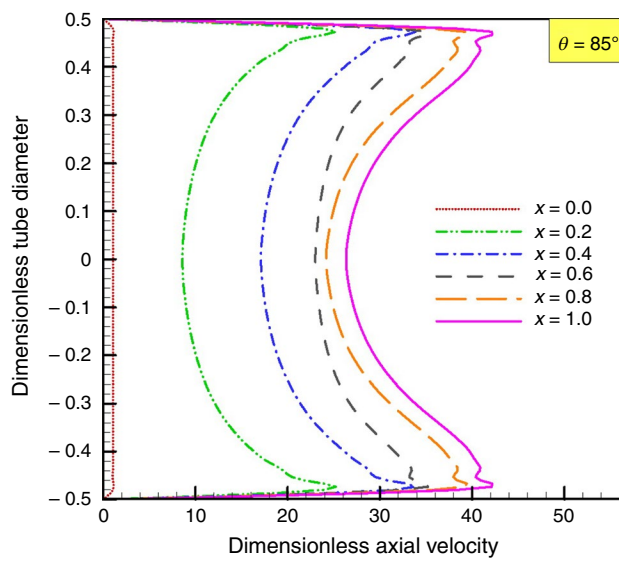


**Fig. 24** Changes in the velocity of the flow over the diameter in terms of the dimensionless distances at temperature difference of 300 °C and 85° angle

mass flow rate of the fluid has been increased from 0.05 to 0.09 kg s<sup>-1</sup>, and the results are shown in Table 9.

As shown, the heat flux increases with increasing mass flux at any angle. The reason for this phenomenon is an increase in the inlet fluid and consequently a greater need for energy to increase the internal energy of the computational cells to break down the molecular bonds. This means that with increasing inlet fluid, more energy is needed to

start the process of mass conversion from liquid phase to vapor phase.

**The effect of average wall temperature change on pressure drop during process**

In this section, the process of changes in pressure drop during the process is studied with changing the temperature difference between the wall and water fluid. As discussed

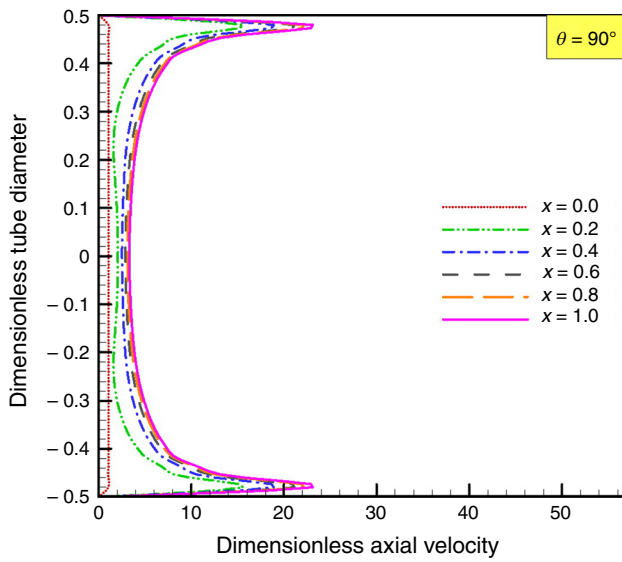


**Fig. 25** Changes in the velocity of the flow over the diameter in terms of the dimensionless distances at temperature difference of 20 °C and 90° angle

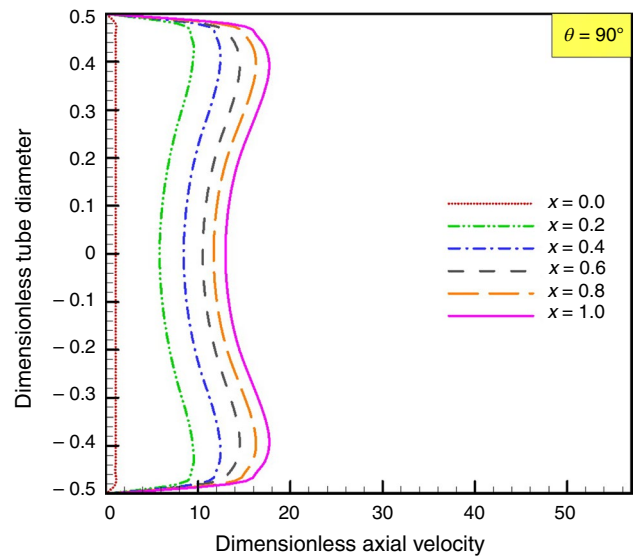


**Fig. 27** Changes in the velocity of the flow over the diameter in terms of the dimensionless distances at temperature difference of 220 °C and 90° angle

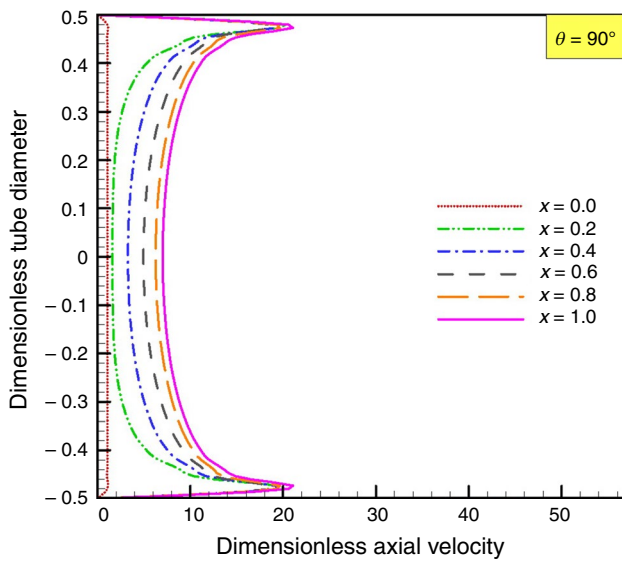


**Fig. 26** Changes in the velocity of the flow over the diameter in terms of the dimensionless distances at temperature difference of 120 °C and 90° angle

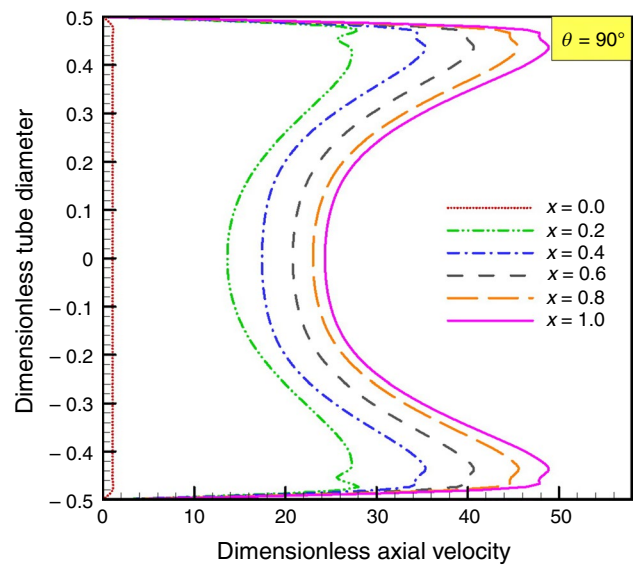


**Fig. 28** Changes in the velocity of the flow over the diameter in terms of the dimensionless distances at temperature difference of 270 °C and 90° angle

in the previous sections, changing the average temperature difference between the wall and fluid increases the critical heat flux. The following equation is used to obtain pressure drop in a tube that constant heat flux is applied to its walls [55]

$$\Delta P = \frac{2f_{f0}G^2v_fL}{D} \left[ \frac{1}{x} \int_0^x \phi_{f0}^2 dx \right] + G^2v_f \left[ \frac{x^2}{\alpha} \left( \frac{v_g}{v_f} \right) + \frac{(1-x)^2}{(1-\alpha)} - 1 \right] + \frac{Lg \sin \theta}{x} \int_0^x [\rho_g \alpha + \rho_f(1-\alpha)] dx \tag{48}$$

**Table 9** Heat flux for different mass flow rates in different angles

Temperature difference value between the wall and fluid/°C	kg s <sup>-1</sup>				
	0.05	0.06	0.07	0.08	0.09
Heat flux/W m <sup>-2</sup>					
80	27,042	46,318	59,342	63,907	86,659
85	33,932	45,150	59,142	68,863	71,375
90	37,104	62,148	78,258	96,163	98,259

This equation, known as Martinelli–Nelson equation [55], contains different sentences of the pressure drop, respectively, from the right, frictional pressure drop, acceleration pressure drop, as well as the gravitational pressure drop, and  $f_{f0}$  is the coefficient of friction of the single-phase fluid flow, which the value is obtained from the following equation [55]:

$$f_{f0} = 0.079Re_f^{-0.025} \tag{49}$$

Since the mass flux, density, viscosity and friction coefficient of the liquid phase at the beginning and end of the process had known and unchanged values, the expressions  $\frac{2f_{f0}G^2v_fL}{D}$  and  $G^2v_f$  are the coefficients of single-phase liquid friction with a constant value. It can be said that the only effective variables affecting the pressure loss equation are the expressions  $\left[ \frac{1}{x} \int_0^x \phi_{f0}^2 dx \right]$  and  $r_2$  which increased, at a given pressure, with increasing heat flux or quality of the outlet vapor (before the critical heat flux), and if heat flux increases, it can be said that the quality of the outlet vapor increases, which means increasing the two variables affects the pressure drop.

We found from Eq. (48) that with increasing the average temperature difference between the wall and fluid, the pressure drop to 320 °C increases. However, this continues with this process only as long as the average temperature difference between the wall and fluid reaches its value before reaching the critical heat flux. After that, it goes against the original process. Figures 29–31 show the effect of changing the average temperature of the wall and fluid on the pressure drop during the process at 80° to 90° angles.

As shown in these figures, with increasing heat flux of the wall and two-phase patterns’ formation in lesser lengths than the beginning of the process, the pressure drop increased during the process, but after the critical heat flux suddenly, this changes, and then the pressure drop reduced sharply, and with increasing the slope of the tube, the pressure drop is increasing. The reason for this is that with increasing heat flux of the wall, the quality of the outlet vapor is increasing, and the increase in the quality of the outlet vapor also means increasing the pressure drop during the process with increasing the flux. The reason for the sudden change in the

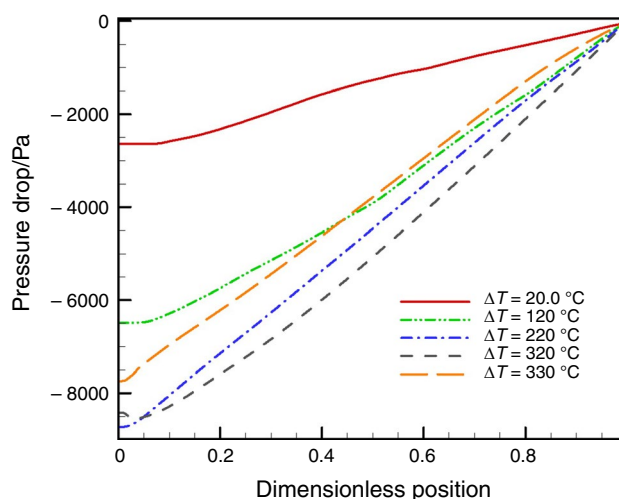


**Fig. 29** Effect of changing the average temperature of the wall and fluid on the pressure drop during the process at 80° angles

pressure drop after the critical heat flux is the occurrence of critical heat flux, which results in a significant reduction in the volume fraction of the outlet vapor phase.

### Conclusions

In this paper, numerical simulation of critical heat flux in forced boiling of a flow in an inclined tube with different angles was investigated. Numerical simulation of fluid was done by using the RPI subcategory of boiling from the Eulerian model, and the comparison of numerical results with

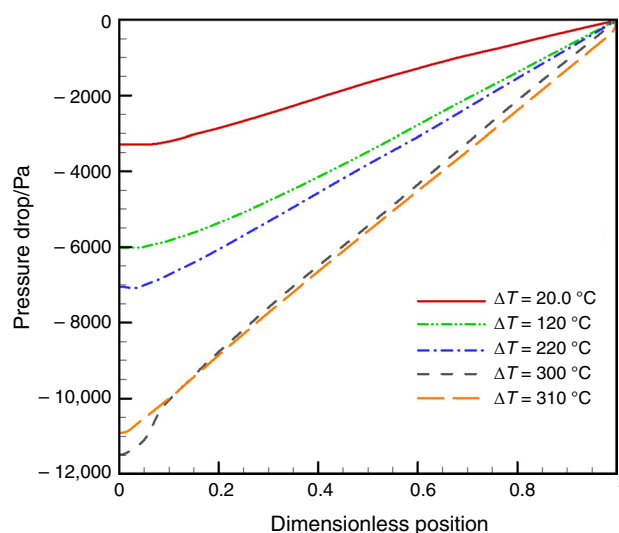


**Fig. 30** Effect of changing the average temperature of the wall and fluid on the pressure drop during the process at 85° angle

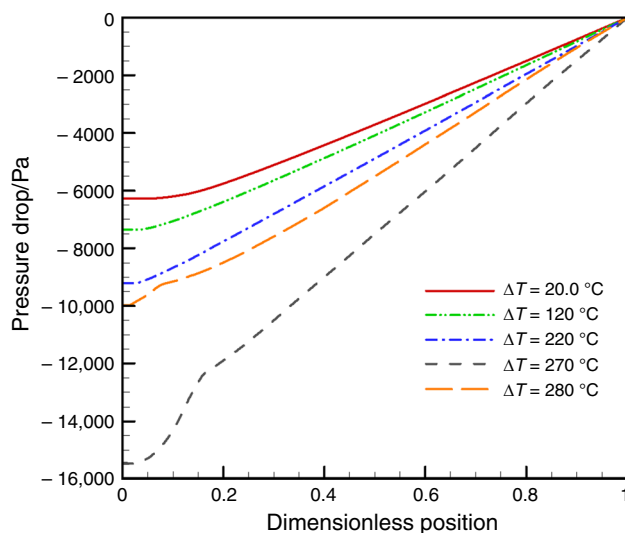


**Fig. 31** Effect of changing the average temperature of the wall and fluid on the pressure drop during the process at 90° angles

valid experimental data shows 14% of error. The following results can be deduced from this study:

- With increasing the temperature difference between the wall and inlet fluid, the velocity magnitude increases.
- By comparing the velocity changes in each temperature to the temperature before it is found that as the temperature increases, the difference in velocity reduced in the wall and in the center of the tube, and at all temperatures, the velocity profile increased to the end of the tube.
- With increasing the tube angle, the higher volume fraction of the vapor phase occurs at a lower temperature due to the rapid changes in the flow pattern due to the increased slope and faster phase conversion from liquid to vapor
- An increase in the wall and fluid temperature difference increases the heat transfer to the liquid and the molecular movement, resulting in the breakdown of the intermolecular fluid links and the conversion of the liquid phase to the vapor phase.
- The increasing process of volume fraction of the vapor has reached a temperature difference of 320 °C to its extreme limit, among other differences in the temperatures studied.

## References

1. Bastas N, Giazitzidis P, Maragakis M, Kosmidis K. Explosive percolation: unusual transitions of a simple model. *Physica A Stat Mech Appl.* 2014;407:54–65.
2. Bonini M, Wiedenmann A, Baglioni P. Synthesis and characterization of surfactant and silica-coated cobalt ferrite nanoparticles. *Physica A Stat Mech Appl.* 2004;339:86–91.
3. Chakrabarti AS. Effects of the turnover rate on the size distribution of firms: an application of the kinetic exchange models. *Physica A Stat Mech Appl.* 2012;391:6039–50.
4. Inaoka H, Ito N. Numerical simulation of pool boiling of a Lennard–Jones liquid. *Physica A Stat Mech Appl.* 2013;392:3863–8.
5. Makowiec D, Dąbkowski J, Groth M. The Eve effect in the Penna model of biological ageing. *Physica A Stat Mech Appl.* 1999;273:169–81.
6. Martyushev LM, Birzina AI, Soboleva AS. On the morphological instability of a bubble during inertia-controlled growth. *Physica A Stat Mech Appl.* 2018;499:170–5.
7. Materassi D, Innocenti G. Unveiling the connectivity structure of financial networks via high-frequency analysis. *Physica A Stat Mech Appl.* 2009;388:3866–78.
8. Roehner BM. How can one explain changes in the monthly pattern of suicide? *Physica A Stat Mech Appl.* 2015;424:350–62.
9. Toghianiyan A, Zarringhalam M, Akbari OA, Sheikh Shabani GA, Toghraie D. Application of lattice Boltzmann method and spinodal decomposition phenomenon for simulating two-phase thermal flows. *Physica A Stat Mech Appl.* 2018;509:673–89.
10. Zhou W-X, Sornette D. Testing the stability of the 2000 US stock market “antibubble”. *Physica A Stat Mech Appl.* 2005;348:428–52.
11. Nasiri H, Abdollahzadeh Jamalabadi MY, Sadeghi R, Safaei MR, Nguyen TK, Safdari Shadloo M. A smoothed particle hydrodynamics approach for numerical simulation of nano-fluid flows. *J Therm Anal Calorim.* 2019;135(3):1733–41. <https://doi.org/10.1007/s10973-018-7022-4>.
12. Yang L, Xu J, Du K, Zhang X. Recent developments on viscosity and thermal conductivity of nanofluids. *Powder Technol.* 2017;317:348–69.
13. Afrand M. Using a magnetic field to reduce natural convection in a vertical cylindrical annulus. *Int J Therm Sci.* 2017;118:12–23.
14. Hopp-Hirschler M, Shadloo MS, Nieken U. Viscous fingering phenomena in the early stage of polymer membrane formation. *J Fluid Mech.* 2019;864:97–140.
15. Yang L, Huang J-n, Ji W, Mao M. Investigations of a new combined application of nanofluids in heat recovery and air purification. *Powder Technol.* 2020;360:956–966.
16. Nguyen MQ, Shadloo MS, Hadjadj A, Lebon B, Peixinho J. Perturbation threshold and hysteresis associated with the transition to turbulence in sudden expansion pipe flow. *Int J Heat Fluid Flow.* 2019;76:187–96.
17. Yang L, Du K, Zhang Z. Heat transfer and flow optimization of a novel sinusoidal minitube filled with non-Newtonian SiC/EG-water nanofluids. *Int J Mech Sci.* 2020;168:105310.
18. Piquet A, Zebiri B, Hadjadj A, Safdari Shadloo M. A parallel high-order compressible flows solver with domain decomposition method in the generalized curvilinear coordinates system. *Int J Numer Methods Heat Fluid Flow.* 2019;ahead-of-print.
19. Yang L, Du K. A comprehensive review on the natural, forced, and mixed convection of non-Newtonian fluids (nanofluids) inside different cavities. *J Therm Anal Calorim.* 2019. <https://doi.org/10.1007/s10973-019-08987-y>.
20. Yang L, Huang J-N, Mao M, Ji W. Numerical assessment of Ag-water nano-fluid flow in two new microchannel heatsinks: thermal performance and thermodynamic considerations. *Int Commun Heat Mass Transf.* 2020;110:104415.
21. Yang L, Ji W, Huang J-n, Xu G. An updated review on the influential parameters on thermal conductivity of nano-fluids. *J Mol Liq.* 2020;296:104415.
22. Yang L, Ji W, Zhang Z, Jin X. Thermal conductivity enhancement of water by adding graphene nano-sheets: consideration of particle loading and temperature effects. *Int Commun Heat Mass Transfer.* 2019;109:104353.
23. Safdari Shadloo M. Numerical simulation of compressible flows by lattice Boltzmann method. *Numer Heat Transf Part A Appl.* 2019;75(3):167–82.

24. Yang L, Mao M, Huang J-N, Ji W. Enhancing the thermal conductivity of SAE 50 engine oil by adding zinc oxide nano-powder: an experimental study. *Powder Technol.* 2019;356:335–41.
25. Shenoy DV, Shadloo MS, Peixinho J, Hadjadj A. Direct numerical simulations of laminar and transitional flows in diverging pipes. *Int J Numer Methods Heat Fluid Flow.* 2019;ahead-of-print.
26. Alsarraf J, Moradikazerouni A, Shahsavari A, Afrand M, Salehipour H, Tran MD. Hydrothermal analysis of turbulent boehmite alumina nanofluid flow with different nanoparticle shapes in a minichannel heat exchanger using two-phase mixture model. *Phys A.* 2019;520:275–88.
27. Liu WI, Alsarraf J, Shahsavari A, Rostamzadeh M, Afrand M, Nguyen TK. Impact of oscillating magnetic field on the thermal conductivity of water–Fe<sub>3</sub>O<sub>4</sub> and water–Fe<sub>3</sub>O<sub>4</sub>/CNT ferro-fluids: experimental study. *J Magn Magn Mater.* 2019;484:258–65.
28. Karimi A, Al-Rashed AAAA, Afrand M, Mahian O, Wongwises S, Shahsavari A. The effects of tape insert material on the flow and heat transfer in a nanofluid-based double tube heat exchanger: two-phase mixture model. *Int J Mech Sci.* 2019;156:397–409.
29. Shahsavari A, Bagherzadeh SA, Mahmoudi B, Hajizadeh A, Afrand M, Nguyen TK. Robust weighted least squares support vector regression algorithm to estimate the nanofluid thermal properties of water/graphene oxide-silicon carbide mixture. *Phys A.* 2019;525:1418–28.
30. Al-Rashed AAAA, Shahsavari A, Akbari M, Toghraie D, Akbari M, Afrand M. Finite volume simulation of mixed convection in an inclined lid-driven cavity filled with nanofluids: effects of a hot elliptical centric cylinder, cavity angle and volume fraction of nanoparticles. *Phys A.* 2019;527:121122.
31. Liu WI, Al-Rashed AAAA, Alsagri AS, Mahmoudi B, Shahsavari A, Afrand M. Laminar forced convection performance of non-Newtonian water–CNT/Fe<sub>3</sub>O<sub>4</sub> nano-fluid inside a minichannel hairpin heat exchanger: effect of inlet temperature. *Powder Technol.* 2019;354:247–58.
32. Alsarraf J, Rahmani R, Shahsavari A, Afrand M, Wongwises S. Effect of magnetic field on laminar forced convective heat transfer of MWCNT–Fe<sub>3</sub>O<sub>4</sub>/water hybrid nanofluid in a heated tube. *J Therm Anal Calorim.* 2019;137:1809–25.
33. Shahsavari A, Baseri MH, Al-Rashed AAAA, Afrand M. Numerical investigation of forced convection heat transfer and flow irreversibility in a novel heatsink with helical microchannels working with biologically synthesized water–silver nano-fluid. *Int Commun Heat Mass Transfer.* 2019;108:104324.
34. Liu W, Shahsavari A, Barzinjy A, Al-Rashed AAAA, Afrand M. Natural convection and entropy generation of a nanofluid in two connected inclined triangular enclosures under magnetic field effects. *Int Commun Heat Mass Transf.* 2019;108:104309.
35. Al-Rashed AAAA, Sheikhzadeh GA, Aghaei A, Monfared F, Shahsavari A, Afrand M. Effect of a porous medium on flow and mixed convection heat transfer of nanofluids with variable properties in a trapezoidal enclosure. *J Therm Anal Calorim.* 2019. <https://doi.org/10.1007/s10973-019-08404-4>.
36. Alsarraf J, Shahsavari A, Khaki M, Ranjbarzadeh R, Karimipour A, Afrand M. Numerical investigation on the effect of four constant temperature pipes on natural cooling of electronic heat sink by nanofluids: a multifunctional optimization. *Adv Powder Technol.* 2019. <https://doi.org/10.1016/j.apt.2019.10.035>.
37. Chen Z, Shahsavari A, Alrashed AAAA, Afrand M. The impact of sonication and stirring durations on the thermal conductivity of alumina-liquid paraffin nanofluid: an experimental assessment. *Powder Technol.* 2019. <https://doi.org/10.1016/j.powtec.2019.11.036>.
38. Ma J, Shahsavari A, Al-Rashed AAAA, Karimipour A, Yarmand H, Rostami S. Viscosity, cloud point, freezing point and flash point of zinc oxide/SAE50 nanolubricant. *J Mol Liq.* 2019. <https://doi.org/10.1016/j.molliq.2019.112045>.
39. Ma Y, Shahsavari A, Moradi I, Rostami S, Moradikazerouni A, Yarmand H, Zulkifli NWBM. Using finite volume method for simulating the natural convective heat transfer of nano-fluid flow inside an inclined enclosure with conductive walls in the presence of a constant temperature heat source. *Phys A.* 2019. <https://doi.org/10.1016/j.physa.2019.123035>.
40. Talebizadehsardari P, Shahsavari A, Toghraie D, Barnoon P. An experimental investigation for study the rheological behavior of water–carbon nanotube/magnetite nanofluid subjected to a magnetic field. *Phys A.* 2019;534:122129.
41. Pezo Milada, Stevanovic Vladimir. Numerical prediction of critical heat flux in pool boiling with the two-fluid model. *Int J Heat Mass Transf.* 2011;54:3296–303.
42. Konishi Christopher, Mudawar Issam. Review of flow boiling and critical heat flux in microgravity. *Int J Heat Mass Transf.* 2015;80:469–93.
43. Sadaghiani AK, Kosar A. Numerical and experimental investigation on the effects of diameter and length on high mass flux subcooled flow boiling in horizontal microtubes. *Int J Heat Mass Transf.* 2016;92:824–37.
44. Lee JS, Lee JS. Critical heat flux enhancement of pool boiling with adaptive fraction control of patterned wettability. *Int J Heat Mass Transf.* 2016;96:504–12.
45. Fang X, Chen Y, Zhang H, Chen W, Dong A, Wang R. Heat transfer and critical heat flux of nanofluid boiling: a comprehensive review. *Renew Sustain Energy Rev.* 2016;62:924–40.
46. Chernyavskiy AN, Pavlenko AN. Numerical simulation of heat transfer and determination of critical heat fluxes at nonsteady heat generation in falling wavy liquid films. *Int J Heat Mass Transf.* 2017;105:648–54.
47. Sato Y, Niceno B. Pool boiling simulation using an interface tracking method: from nucleate boiling to film boiling regime through critical heat flux. *Int J Heat Mass Transf.* 2018;125:876–90.
48. Ferrari A, Magnini M, Thome JR. Numerical analysis of slug flow boiling in square microchannels. *Int J Heat Mass Transf.* 2018;123:928–44.
49. Wang J, Diao M, Liu X. Numerical simulation of pool boiling with special heated surfaces. *Int J Heat Mass Transf.* 2019;130:460–8.
50. Cheng N, Guo Y, Peng C. A numerical simulation of single bubble growth in subcooled boiling water. *Ann Nucl Energy.* 2019;124:179–86.
51. Akhgar A, Davood T, Nima S, Masoud A. Developing dissimilar artificial neural networks (ANNs) to prediction the thermal conductivity of MWCNT–TiO<sub>2</sub>/Water-ethylene glycol hybrid nanofluid. *Powder Technol.* 2019;355:602–610.
52. Cable Matt. An evaluation of turbulence models for the numerical study of forced and natural convective flow in Atria. Ontario: Queen's University Kingston; 2009.
53. James ME, Papavassiliou DV, O'Rear EA. Use of computational fluid dynamics to analyze blood flow, hemolysis and sublethal damage to red blood cells in a bileaflet artificial heart valve. *Fluids.* 2019;4(1):19.
54. Mosaad M, Johannsen K. Experimental study of steady-state film boiling heat transfer of subcooled water flowing upwards in a vertical tube. *Exp Therm Fluid Sci.* 1989;2(4):477–93.
55. Collier JG, Thome JR. Convective boiling and condensation. Oxford: Oxford University Press; 1994.

**Publisher's Note** Springer Nature remains neutral with regard to jurisdictional claims in published maps and institutional affiliations.